Title
Modeling Solute-Dislocation Interactions in Body-Centered Cubic Alloys Using Kinetic Monte Carlo Simulations

Author
ZHAO, YUE

Publication Date
2019

Peer reviewed|Thesis/dissertation

UNIVERSITY OF CALIFORNIA

Los Angeles

Modeling Solute-Dislocation Interactions in Body-Centered Cubic Alloys Using Kinetic Monte Carlo Simulations

A dissertation submitted in partial satisfaction
of the requirements for the degree
Doctor of Philosophy in Materials Science and Engineering

by

Yue Zhao

2019

ABSTRACT OF THE DISSERTATION

Modeling Solute-Dislocation Interactions in Body-Centered Cubic Alloys Using Kinetic Monte Carlo Simulations

by

Yue Zhao
Doctor of Philosophy in Materials Science and Engineering
University of California, Los Angeles, 2019
Professor Jaime Marian, Co-Chair
Professor Lucile Dezerald, Co-Chair

Interactions among dislocations and solute atoms are the basis of several important processes in metal plasticity. In body-centered cubic (bcc) metals and alloys, low-temperature plastic flow is controlled by screw dislocation glide, which is known to take place by the nucleation and sideward relaxation of kink pairs across two consecutive Peierls valleys. In alloys, dislocations and solutes affect each others kinetics via long-range stress field coupling and short-range inelastic interactions. It is known that in certain substitutional bcc alloys a transition from solute softening to solute hardening is observed at a critical concentration. In the first part of this work, we develop a kinetic Monte Carlo model of screw dislocation glide and solute diffusion in substitutional W–Re alloys. We find that dislocation kinetics is governed by two competing mechanisms. At low solute concentrations, nucleation is enhanced by the softening of the Peierls stress, which dominates over the elastic repulsion of Re atoms on kinks. This trend is reversed at higher concentrations, resulting in a minimum in the flow stress that is concentration and temperature dependent. This minimum marks the transition from solute softening to hardening, which is found to be in reasonable agreement with experiments.

In the second part of this work, we extend our model to interstitial W–O alloys. we report

for the first time on simulations of jerky flow in W-O as a representative bcc interstitial solid solution. The simulations are carried out in a stochastic framework that naturally captures rare events in a rigorous manner, enabling the study of solute diffusion and dislocation motion concurrently. The model has no adjustable parameters, with all coefficients calculated using first principles methods. We find that three regimes emerge from the stress-temperature space: one representative of standard solid solution strengthening, another mimicking solute cloud formation, and a third one, where the dynamic interaction of solutes and dislocations results in jerky flow and dynamic strain aging. We show how the symbiosis between quantum mechanical calculations and mesoscopic methods capable of furnishing diffusive timescales is a powerful demonstration of the capacities of physical models to explain macroscopic behavior.

The dissertation of Yue Zhao is approved.

Ali Mosleh

Dwight C. Streit

Jaime Marian, Committee Co-Chair

Lucile Dezerald, Committee Co-Chair

University of California, Los Angeles

2019

To my dear mother Houfang Liu

To my dear father Changshi Zhao

Contents

List of Figures

Acknowledgments

It's been 21 years since a little boy walked into the elementary school for the first time. Now it's time for him to walk out of UCLA campus soon with a doctorate and an enthusiastic heart of learning that has never been changed. I first want to thank him for his passion and hard-working.

Second, I want to thank my mother Houfang Liu and my father changshi Zhao. It's you who raise my up and raise my up to more than I can be. I love you. I also want to thank my dear Tingyu Bai. It's your company that walk me through all the difficulties.

Third, I want to thank Professor Jaime Marian. You teach me not only how to do research but also how to be a gentle man. I cannot remember how many times I said "I appreciate it" to you. But I want to say again that I appreciate all the things you have done for me. I will put them in my heart. I also want to thank Professor Lucile Dezerald for collaboration in research, beers and happy time in Nancy.

Last, I want to thank my best friend Miao Lin, Tianyi Zhang, Xiaomeng Hu, Jingqiu Tang, Pengchao Xu and Jiqun Tu. I also want to thank people in Marian's group, especially, Hsing-Yin Chang and Chen-Hsi Huang. Finally, I want to thank all the people who have helped me.

The author acknowledge support by the National Science Foundation under Grant DMR-1611342 and the U.S. Department of Energys Office of Fusion Energy Sciences, Project DE-SC0012774:0001. This work was also supported by the French State through the program Investment in the future operated by the National Research Agency (ANR) and referenced by ANR-11-LABX-0008-01 (LabEx DAMAS). Computer time allocations at UCLAs IDRE Hoffman2 supercomputer are acknowledged. Part of this research was also performed using HPC resources from GENCI-CINES and TGCC from CEA under Grants 2016-097647, A0020910156, and A0040910156, as well as from PRACE (Partnership for Advanced Computing in Europe) access to the AIMODIM project.

Curriculum Vitae

2014 – Present	Ph.D. candidate in Materials Science and Engineering, University of California, Los Angeles (UCLA).
2010 – 2014	B.S. in Physics, Fudan University, Shanghai, China.
2016 – 2017	University Fellowship, UCLA.
2015	The First Prize Undergraduate Scholarship, Fudan University.
2009	First Prize, National High School Physics Competition, China.

Publications

[1] Yue Zhao, Lucile Dezerald, and Jaime Marian. Electronic structure calculations of oxygen atom transport energetics in the presence of screw dislocations in tungsten. *Metals*, 9(2):252, 2019.

[2] Yue Zhao and Jaime Marian. Direct prediction of the solute softening-to-hardening transition in w–re alloys using stochastic simulations of screw dislocation motion. *Modelling and Simulation in Materials Science and Engineering*, 26(4):045002, 2018.

[3] Chen-Hsi Huang, Leili Gharaee, Yue Zhao, Paul Erhart, and Jaime Marian, "Mechanism of nucleation and incipient growth of Re clusters in irradiated W-Re alloys from kinetic Monte Carlo simulations," Phys. Rev. **B96**, 115005 (2017) .

CHAPTER 1

Introduction

Tungsten(W) is one of the most promising material for fusion application, due to its high strength and excellent high temperature properties [7, 37, 110, 163]. W and its alloys have been widely discussed and investigated as the helium-cooled divertor and the protection of the helium-cooled first wall in reactor designs going beyond ITER [9, 48, 55, 96, 116]. However, The applications of W have been limited to a great extent by their brittleness at ambient temperatures [105, 130]. In order to increase the ductility, Rhennium(Re) is by now the only element(or probably Iridium) can be used to form ductile tungsten alloys. W is typically alloyed with 5-26 at.% Re to increase low temperature ductility and improve high temperature strength and plasticity, which can increase K_c by up to one order of magnitude [35, 88]. However, the cost and irradiation embrittlement of W–Re alloys has limited its use for fusion energy applications [74]. Understanding the physical reasons behind the Re-induced ductilization can be helpful to improve the application of W–Re alloy and find other suitable W-based alloys.

The physical origins behind the Re-induced ductilization have been discussed in the literature [75, 114, 130, 154] and point in some way or another to alterations in the core structure of $\frac{1}{2}\langle 111\rangle$ screw dislocations, which both reduce the effective Peierls stress and extend the number of possible slip pathways. However, this is a highly local effect, concentrated around the vicinity of screw dislocation cores, whereas plasticity involves both long-range and local solute-core interactions. Although the softening of the Peierls stress, σ_P, can be expected to lead to an increased screw dislocation mobility, factors such as kink-pair nucleation enthalpies and kink velocities must be considered to accurately assess whether Re additions result in global solute softening, hardening, or both. This was recognized early

on for body-centered cubic (bcc) alloys in the experimental literature, where there is ample evidence of a transition from solute softening to solute strengthening in substitutional alloys [42,66,75,94,100,107,108]. This transition is usually rationalized as a competition between kink-pair nucleation and kink motion, which are thought to depend inversely on solute content. Although early models built on this idea to successfully predict the softening-to-hardening transition [58, 121], it was not until very recently that sophisticated electronic structure calculations have revealed the local effect of Re alloying on the structure of screw dislocation cores in W [68,114,118,154]. The effect on solute migration of dislocation stress fields can now also be characterized by combining elasticity theory with electronic structure calculations [49,51,137,156]. In the first part of this work, we attempt to provide a multi-scale modeling of the plastic properties of W based alloys from atomistic electronic structure calculations of the dislocation core interaction with solute atoms to the screw dislocation movement. We develop a kinetic Monte Carlo (kMC) model that accounts for thermally-activated kink-pair nucleation and solute diffusion via stress-field coupling and short-range inelastic interactions. Within our model the solute subsystem and the dislocation evolve in a coupled fashion, with solute diffusion being sensitive to dislocation stress fields, and kink-pair nucleation and propagation being influenced by the presence of solute. Our model is parameterized entirely using electronic structure calculations, as described by Hossain and Marian [49], and is significantly more efficient than direct atomistic simulations. This allows us to study the relevant parameter space of stress, temperature, Re content, and dislocation line length by simulating the motion of a screw dislocation in a random W-Re solid solution.

Most usable metallic materials are cast as alloys, containing one or more elements in concentrations ranging from trace amounts of solute up to several ten percent. Due to their extraordinary importance in technology and society, understanding the mechanical behavior of alloys is a primary research goal of the materials science community. Preventing plastic localization is a chief concern of researchers to avoid brittle failure, and substantial efforts have been devoted over the years to study processes that lead to localized deformation. The Portevin-Le Chatelier (PLC) effect is one such phenomenon that occurs in certain metallic

alloys by which plastic slip becomes unstable, resulting in serrated flow and the onset of inhomogeneous deformation. The PLC effect is a well-known phenomenon in materials science by which metallic alloys deform in an unstable manner, potentially leading to poor ductility and premature failure [2,3,12,59,62,72,80,86,89,90,92,93,98,103,104,134,153,157]. Serrated flow is thought to be due to the dynamic interplay between dislocations and solute atoms, which is favored in a particular temperature and strain rate regime. This interplay is almost always inaccessible experimentally, which calls for the development of physical models capable of bridging the relevant temporal and spatial scales involved in the process. However, while phenomenological models of serrated flow have existed since the first observation of the phenomenon, the direct simulation of the PLC effect in three dimensions has eluded the materials and metallurgical science community for years. The difficulties to simulate serrated flow are aggravated in body-centered cubic (bcc) metals, where the crystal structure of the alloy brings an extra set of complexities that necessitate specific experimental and theoretical treatments. In the second part of this work, we extent our kMC model to the interstitial W–O system. We report for the first time on simulations of jerky flow in W-O as a representative bcc interstitial solid solution. The simulations are carried out in a stochastic framework that naturally captures rare events in a rigorous manner, enabling the study of solute diffusion and dislocation motion concurrently. The model has no adjustable parameters, with all coefficients calculated using first principles methods. We find that three regimes emerge from the stress-temperature space: one representative of standard solid solution strengthening, another mimicking solute cloud formation, and a third one, where the dynamic interaction of solutes and dislocations results in jerky flow and dynamic strain aging. We show how the symbiosis between quantum mechanical calculations and mesoscopic methods capable of furnishing diffusive timescales is a powerful demonstration of the capacities of physical models to explain macroscopic behavior.

In chapter 2, we develop a kinetic Monte Carlo model of screw dislocation glide and solute diffusion in substitutional W–Re alloys. In chapter 3, we use electronic structure calculations to obtain the energetics of oxygen diffusion under stress and its interaction energy with screw

dislocation cores in bcc tungsten. In chapter 4, we extent our kMC model to W–O systems and try to explain the physical reason behind The PLC effect. In chapter 5, we give the explanation and implementation details of Our kMC model.

CHAPTER 2

Direct prediction of the solute softening-to-hardening transition in W-Re alloys using stochastic simulations of screw dislocation motion

2.1 Introduction

The applications of tungsten (W) and its alloys have been limited to a great extent by their brittleness at ambient temperatures. Typical ductile-to-brittle transition temperatures (DBTT) for arc-melted W range from approximately 475 to 525 K, whereas for wrought and recrystallized metal the DBTT falls between 560 to 645 K [105, 130]. Some authors have measured a DBTT in excess of 1000 K for sintered specimens [26,36]. At room temperature, the fracture toughness K_c of polycrystalline W in ranges between 5.1 (sintered) and 9.1 (rolled) MPa$\cdot\sqrt{\text{m}}$ [44]. W is typically alloyed with 5-26 at.% Re to increase low temperature ductility and improve high temperature strength and plasticity, which can increase K_c by up to one order of magnitude [35, 88].

The purpose of this study is to predict the softening-to-hardening transition in W-Re alloys by directly simulating the interaction of screw dislocations with solute atoms. We develop a kinetic Monte Carlo (kMC) model that accounts for thermally-activated kink-pair nucleation and solute diffusion via stress-field coupling and short-range inelastic interactions. Within our model the solute subsystem and the dislocation evolve in a coupled fashion, with solute diffusion being sensitive to dislocation stress fields, and kink-pair nucleation and propagation being influenced by the presence of solute. Our model is parameterized entirely using electronic structure calculations, as described by Hossain and Marian [49],

and is significantly more efficient than direct atomistic simulations. This allows us to study the relevant parameter space of stress, temperature, Re content, and dislocation line length by simulating the motion of a screw dislocation in a random W-Re solid solution. In Section 2.2, we provide a description of the methods employed, followed by the results of dislocation mobility and critical stresses in Section 2.3. We conclude in Section 2.4 with a discussion of our findings and the conclusions.

2.2 Numerical model and parameterization

Detailed descriptions of the kMC model and the electronic structure calculations of model parameters have been published previously [49,133], and here we simply provide a brief review and highlight the aspects that are most relevant to the coupling between the dislocation and the solute subsystem. Suffice it to say that our approach is a three-dimensional, full-elasticity model of arbitrary dislocation geometries in bcc lattices.

2.2.1 Effect of solute on kink-pair activation enthalpy

We start with the expression for the nucleation rate of a kink pair on a screw dislocation segment in the pure material:

$$r_{kp} = \nu_0 \frac{L-w}{b} \exp\left(-\frac{\Delta H(\boldsymbol{\sigma})}{kT}\right) \tag{2.1}$$

where ν_0 is an attempt frequency, L is the available segment length, w is the kink pair separation, $b = a\sqrt{3}/2$ is the modulus of the Burgers vector $\vec{b}$ (a is the lattice parameter), ΔH is the activation enthalpy, which is a function of the local stress tensor $\boldsymbol{\sigma}$, k is Boltzmann's constant and T is the absolute temperature. For its part, the kink-pair activation enthalpy is assumed to follow the expression:

$$\Delta H(\boldsymbol{\sigma}) = \Delta H_0 \left(1 - [\Theta(\boldsymbol{\sigma})]^p\right)^q \tag{2.2}$$

where is ΔH_0 the sum of the formation enthalpy of two opposite-signed kinks, $\Theta(\boldsymbol{\sigma})$ is a *stress ratio* that depends on $\boldsymbol{\sigma}$, and p and q are fitting parameters. The stress ratio is defined

as:

$$\Theta(\boldsymbol{\sigma}) = \frac{\tau_{MRSS}}{\tau_c(\boldsymbol{\sigma})} \tag{2.3}$$

where τ_{MRSS} is the *maximum* resolved shear stress (MRSS) and $\tau_c(\boldsymbol{\sigma})$ is the critical stress for athermal dislocation motion. The stress factor includes in its formulation all non-Schmid effects characteristic of bcc metals, given below.

Equation (2.2) is modified by the presence of solute. Specifically, when a Re atom is found adjacent to the dislocation line, an extra (binding) energy has to be overcome to nucleate the next kink-pair along that dislocation segment. This is shown in Figure 2.1, where a Re atom is along the path of the dislocation. In such case, eq. (2.2) is modified as:

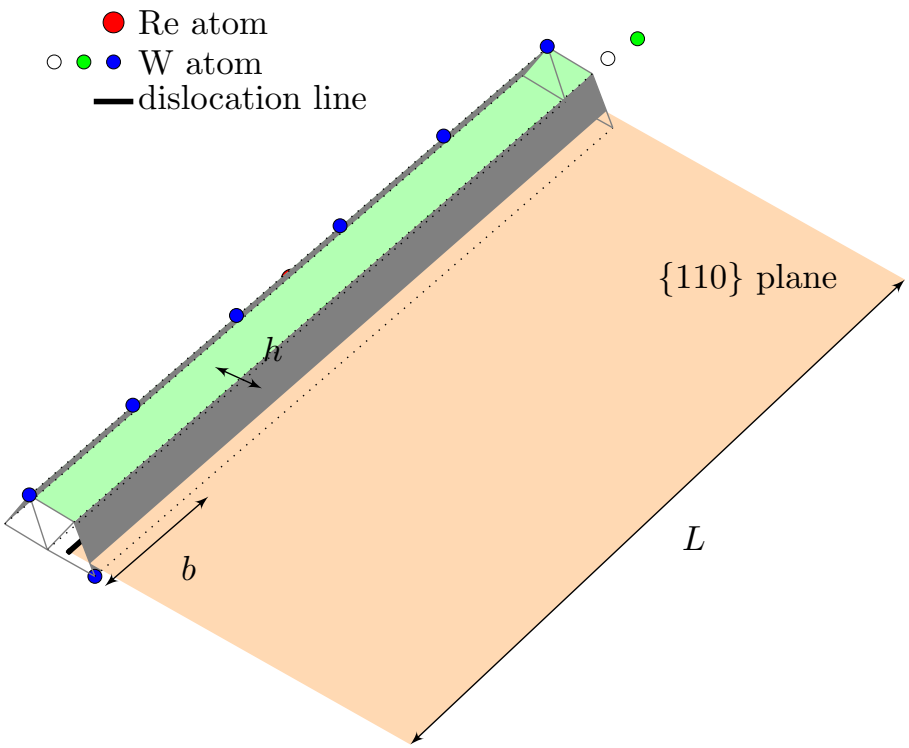

Figure 2.1: Position of lattice atoms relative to a screw dislocation segment of length L containing a kink-pair. The presence of a Re atom (red sphere) changes the activation enthalpy of subsequent kink-pair nucleation events. W atoms are colored according to the $\langle 111 \rangle$ string they belong to.

$$\Delta H'(\boldsymbol{\sigma}) = e_b^{kp} + \Delta H(\boldsymbol{\sigma}) \tag{2.4}$$

The binding energy e_b^{kp} depends on the distance and position of the solute atom relative to the dislocation core, and we have calculated it using DFT calculations [49]. It takes a value of 0.25 eV for the configuration shown in Fig. 2.1 and decays quickly to zero thereafter, taking a value of 0.04 eV for the next nearest atomic row.

2.2.2 Effect of solute on kink motion

In the pure metal, kinks move along the dislocation line with a velocity:

$$v_{\mathrm{k}} = \frac{bm\sigma\vec{b}}{B} \tag{2.5}$$

where B is a friction coefficient. This reflects the fast viscous motion of nonscrew segments. After nucleation, a kink will take an average time of:

$$\delta t_{\mathrm{k}} = \frac{L-w}{2v_{\mathrm{k}}} = \frac{B(L-w)}{2bm\sigma\vec{b}} \tag{2.6}$$

to sweep half of the segment length of the dislocation. However, when a moving kink encounters a Re atom, it binds to it with an energy that depends on their relative location. From that moment on, kink motion ceases and detachment becomes thermally activated. The corresponding detachment rate is:

$$r_{sk} = \nu_1 \exp\left(-\frac{e_b^{sk}}{kT}\right) \tag{2.7}$$

where v_1 is an attempt frequency (different from ν_0) and e_b^{sk} is the binding energy between the kink segment and the Re atom. Kink segments have partial edge dislocation character and, as such, induce both tensile and compressive stresses. Re atoms are approximately 3% larger than W atoms and therefore introduce a certain dilation strain. Therefore, Re binds preferentially to the tensile lobe of a single kink segment deformation field, with a value of $e_b^{sk} = 0.45$ eV. In any case, the binding energy in the compressive region is also attractive, with a maximum value of 0.35 eV [49]. Thus, for simplicity, we take an average value of 0.40 eV regardless of solute atom relative location. We assume this energy to be independent of stress.

Once a dissociation event occurs for a kink-solute configuration, the kink resumes its viscous motion according to eq. (2.5).

2.2.3 The critical stress and non-Schmid effects

Our model includes non-Schmid effects from both sources commonly considered in the literature: the *twinning/antitwinning* effect and non-glide stresses [46]. We follow our previous work on the topic [20, 102] to define the stress ratio Θ as:

$$\Theta(\boldsymbol{\sigma}) = \frac{\tau_{(\bar{1}01)} + a_1 \tau_{(0\bar{1}1)}}{a_0 \sigma_P(c) f\left(\frac{a_2 \tau'_{(\bar{1}01)} + a_3 \tau'_{(0\bar{1}1)}}{a_0 \sigma_P(c)}\right)} \tag{2.8}$$

where

$$\begin{aligned} \tau_{(\bar{1}01)} &= \boldsymbol{\sigma} : \vec{m}^\alpha \otimes \vec{n}^\alpha \\ \tau_{(0\bar{1}1)} &= \boldsymbol{\sigma} : \vec{m}^\alpha \otimes \vec{n}_1^\alpha \\ \tau'_{(\bar{1}01)} &= \boldsymbol{\sigma} : (\vec{n}^\alpha \times \vec{m}^\alpha) \otimes \vec{n}^\alpha \\ \tau'_{(0\bar{1}1)} &= \boldsymbol{\sigma} : (\vec{n}_1^\alpha \times \vec{m}^\alpha) \otimes \vec{n}_1^\alpha \end{aligned} \tag{2.9}$$

and $f(x) = 2/\left(1 + e^{2x}\right)$ [102]. The vectors $\vec{m}^\alpha$, $\vec{n}^\alpha$, and $\vec{n}_1^\alpha$ refer, respectively, to the slip direction, the glide plane, and the adjacent $\{110\}$ plane forming $+60°$ about the screw direction to the glide plane. α refers to any one of the 12 independent slip systems in the bcc crystal lattice [20]. Figure 2.2 shows the relative geometry for the particular case of the $\frac{1}{2}[111](\bar{1}01)$ slip system. We assume that the only dependence of Θ on the Re concentration c is via an explicit dependence of the Peierls stress on c, which we discuss below.

2.2.4 The Peierls stress

First principles calculations in pure W put the value of the Peierls stress between 1.7 and 2.8 GPa [31, 114, 119]. In this work, the key dependence of σ_P is on the solute concentration, for which we use the calculations by Romaner *et al.* [114] and fit a numerical expression of the type $\sigma_P(c) = \frac{b_1}{c + b_2}$ (where b_1 and b_2 are fitting constants) to their data. This softening of the Peierls stress with Re content, together with a dislocation core transformation, has been used by the authors in ref. [114] to explain the ductilization of W with Re in W-Re alloys.

The fit, shown in Figure 2.3, yields values of $b_1 = 1.07$ (GPa) and $b_2 = 0.51$. This is the

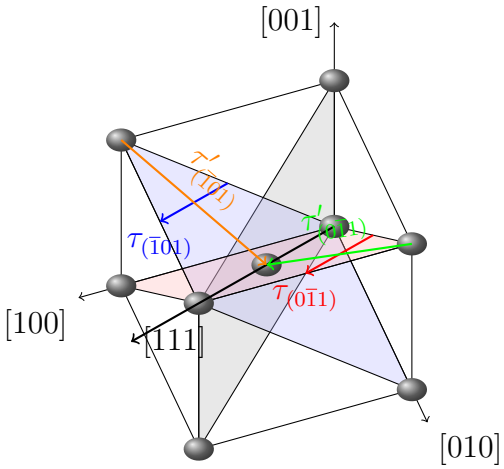

Figure 2.2: Stress projections as defined in eq. (2.9) within the bcc unit cell. The dislocation line is assumed to be along the [111] direction.

expression that we use in the remainder of this paper to carry out our kMC simulations in the presence of solute.

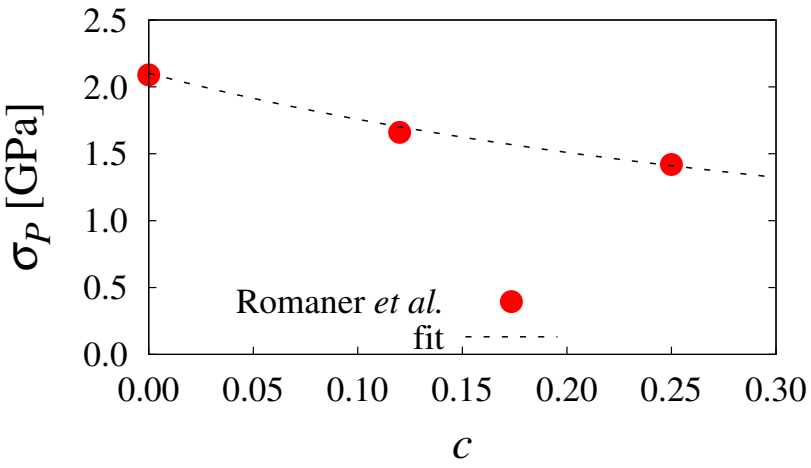

Figure 2.3: Variation of the Peierls stress with Re concentration from ref. [114]. The data points have been fitted to the expression $\sigma_P(c) = \frac{1.07}{c+0.51}$ (in GPa).

2.2.5 Solute diffusion

Re atoms occupying substitutional lattice sites in bcc W can diffuse by thermally activated nearest-neighbor jumps. This jump rate can be expressed as:

$$r_s = \nu_2 \exp\left(-\frac{\Delta H_f^{\mathrm{v}}(\boldsymbol{\sigma}) + H_m(\boldsymbol{\sigma}) + e_b^{\alpha}}{kT}\right) \tag{2.10}$$

where ν_2 is the attempt frequency for vacancy jumps –taken here as the *Debye* frequency, cf. Table 2.1–, ΔH_f^{v} is the vacancy formation enthalpy, ΔH_m is the migration enthalpy, both of which depend on the local stress tensor σ, and e_b^{α} is the binding energy either to a screw segment ($\alpha \equiv \mathrm{k}p$) or to a kink segment ($\alpha \equiv \mathrm{s}k$). This last term is only appropriate when the Re atom is bound to the dislocation core, otherwise it need not be included. The functional dependencies of the activation enthalpies on stress have been given in our previous publication [49], and they are based on the concept of formation or activation volume, which is a tensor defined as;

$$V_{ij}^{*} = \frac{\partial H}{\partial \sigma_{ij}}$$

such that the enthalpy is in general defined as:

$$\Delta H(\boldsymbol{\sigma}) = E - \boldsymbol{\sigma} : \boldsymbol{V}^{*}$$

where the last term in the r.h.s of the above expression is known as the *mechanical work*. The vacancy formation and activation volumes in W-Re alloys have also been calculated in the dilute limit using DFT as given in ref. [49]. In the bcc lattice, each solute atom can jump to eight different nearest neighbor positions, each with its own rate as given by the local stress tensor at each location. To preserve detailed balance in the kMC simulations all eight possible transitions are considered for each Re atom.

The above approach results in tracer diffusion with a drift produced by the dislocation stress field, such that solute diffusion and dislocation motion are coupled to one another. This is the basic premise underlying a series of phenomena categorized under the umbrella of *dynamic strain aging*, whereby coupled dislocation-solute evolution may result in anomalous mechanical behavior.

Table 2.1: Parameter values employed in this work.

Parameter	Units	Value
a	Å	3.16
b	Å	2.74
h	Å	2.58
ν_0	Hz	9.1×10^{11}
ν_1	Hz	1.5×10^{12}
ν_2	Hz	6.4×10^{12}
w	b	11
ΔH_0	eV	1.63
p	-	0.86
q	-	1.69
B	Pa·s	8.3×10^{-5}
a_0	-	1.45
a_1	-	0.99
a_2	-	2.36
a_3	-	4.07
$e_b^{\mathrm{k}p}$	eV	0.25
$e_b^{\mathrm{s}k}$	eV	0.40

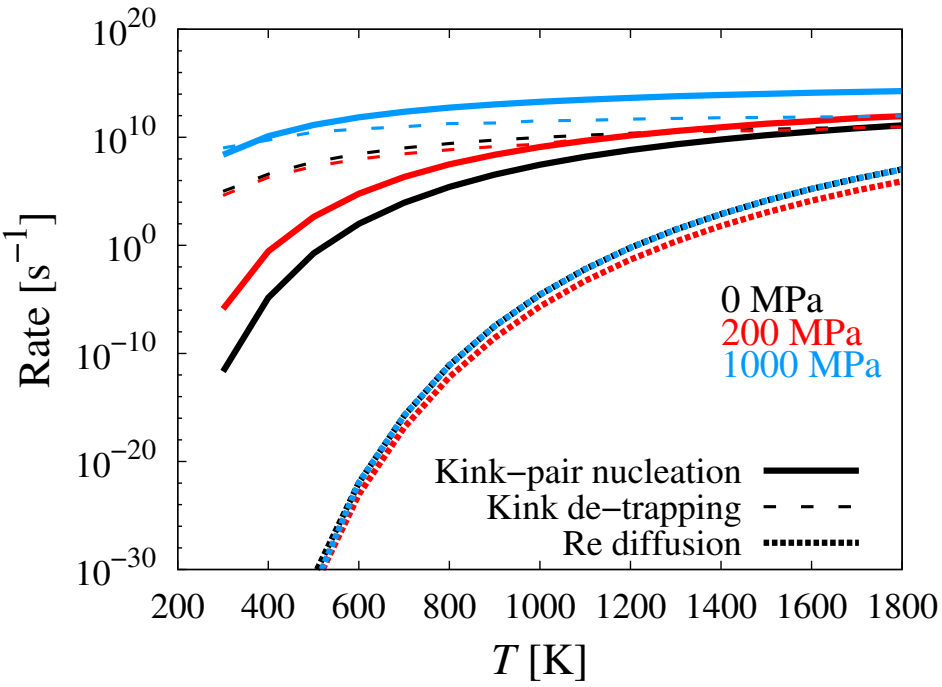

Figure 2.4: Magnitude of the three principal thermally-activated event rates as a function of temperature at three stress points. In the range explored, solute diffusivity is markedly lower than kink-pair nucleation and kink de-trapping.

However, a quick inspection of the three principal thermally-activated event rates, namely kink-pair nucleation, eq. (2.1), kink de-trapping, eq. (2.7), and solute hopping, eq. (2.10) reveals a large gap in time scale between Re atom diffusion and the other two. This is showcased in Figure 2.4, where the rates are plotted as a function of temperature at 0, 200, and 1000 MPa. For this reason, in the following, we neglect solute diffusion and assume that the dislocations move in a static solute field.

2.2.6 Solute distribution spatial update

Our simulations involve periodic boundary conditions along the Burgers vector direction [133], while the other two dimensions are defined by the extent of the solute cloud around the dislocation. For convenience, we construct an hexagonal prism centered along the axis of the center-of-mass (COM) of the dislocation, with edges along the different glide planes of

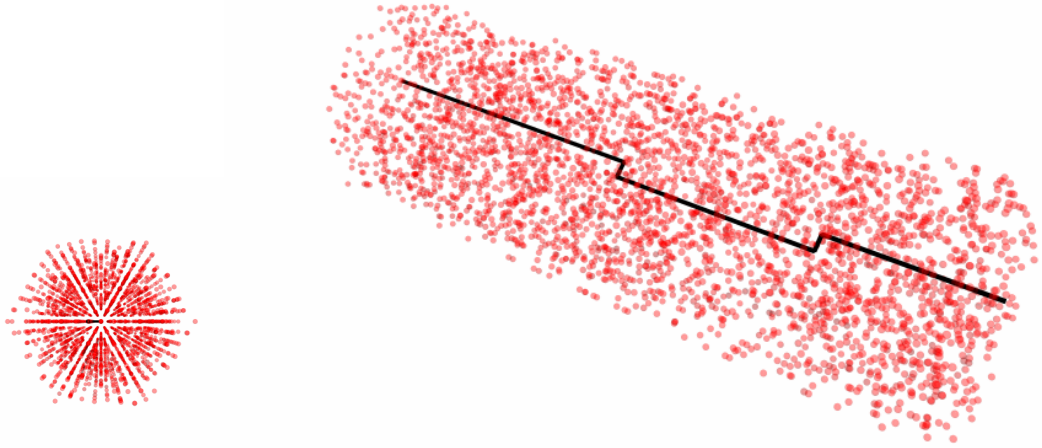

(a) **(b)**

Figure 2.5: Views of the solute prism containing a screw dislocation with a kink pair (a) along the dislocation direction and (b) general view. The images correspond to a simulation at 300 K, 200 MPa of applied stress, and 5% Re concentration.

the [111] zone. Then solute is randomly placed with the appropriate concentration on lattice sites contained within the prism prior to starting the simulations. Because solute strain fields are short-ranged and solute diffusion occurs by way of discrete first-nearest-neighbor jumps, the size of the prism is not very important. Rather, the critical aspect here is to ensure that the prism is updated as the dislocation glides so that 'fresh' material is generated ahead of the dislocation path. This is done to avoid periodic boundary artifacts resulting from prior dislocation-solute interactions. In this fashion, after every time step, the prism is shifted by the amount displaced by the dislocation COM, Re atoms belonging to the previous prism are kept, atoms outside the new prism are discarded, and regions of the prism without solute are populated randomly with the correct c. Figure 2.5 shows images of the solute prism for a dislocation containing a kink-pair in W-5Re (at%).

2.3 Results

The raw output of our method are dislocation velocities as a function of all the internal variables of the model: T, c, $\boldsymbol{\sigma}$, L, and MRSS plane. Here we study the variation of the flow stress with Re content, as the impact of the other variables on dislocation motion has been studied in depth in our previous work [133].

Here we define the flow stress as the stress required to accelerate a screw dislocation to a velocity commensurate with the prescribed strain rate. This velocity can be calculated via Orowan's equation as:

$$v^*(\tau_f) = \frac{\dot{\varepsilon}}{\rho b}$$

where τ_f is the aforementioned flow stress, and ρ is the dislocation density. For the nominal conditions used by Stephens [130], i.e. a strain rate of $\dot{\varepsilon} = 5.5 \times 10^{-4}$ s^{-1}, and a dislocation density $\rho \approx 1.4 \times 10^{14}$ m^{-2}, we obtain a threshold dislocation velocity of 1.5×10^{-8} m s^{-1}. By way of example, we first show screw dislocation velocities as a function of temperature, Re concentration, and MRSS plane in Figure 2.6. For consistency with the experimental measurements, we consider only the case where $L = \rho^{-1/2} \approx 400b$ (≈100 nm), and so we eliminate the dislocation length from consideration as a variable going forward. The figure shows results for 0, 5, and 20% Re concentration at 150, 300, and 590 K. The yellow shaded area marks the region where the dislocation velocity is not fast enough to activate slip, i.e. $v<v^*$, and thus from the intercepts of the velocity curves with the v^* abscissa one can obtain the flow stress τ_f in each case. In other words, we obtain τ_f as the stress above which the dislocation velocity for each simulation triad (L, T, c) is larger than v^*.

It is helpful to consider the analytical analog of this flow stress for 0% Re content to better understand its meaning. A closed-form expression for τ_f can be obtained assuming that the time employed by single kinks to sweep across the dislocation line, δt_{k} (cf. eq. (2.6)), is much shorter than the time required to nucleate kink pairs, $\delta t_{\mathrm{k}} = r_{\mathrm{k}p}^{-1}$ (cf. eq. (2.1)). In such a case, the dislocation velocity can be approximated by [20]:

$$v \approx \frac{\nu_0 h(L-w)}{b} \exp\left\{\frac{\Delta H_0}{kT}\left(1 - \left(\frac{\tau_{\mathrm{RSS}}}{\sigma_P}\right)^p\right)^q\right\} \tag{2.11}$$

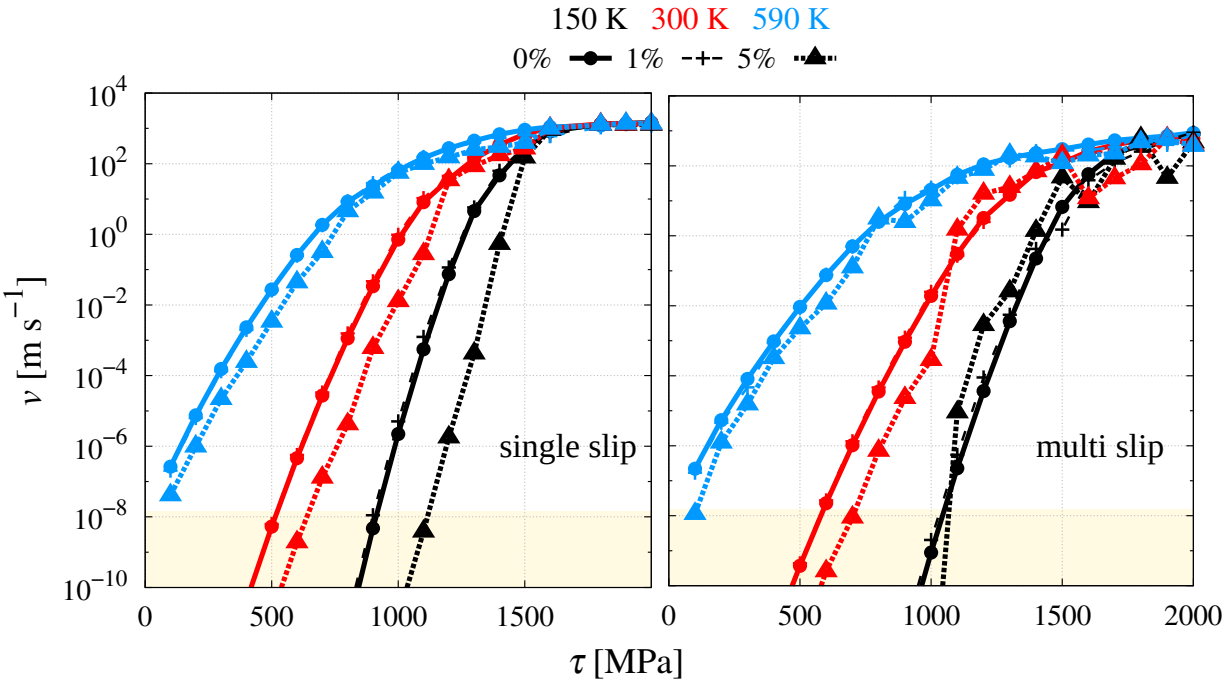

Figure 2.6: Dislocation velocity as a function of stress, temperature, and Re content. The data correspond to a screw dislocation segment $400b$ in length (∼100 nm). Results for (nominally) single slip –MRSS plane is of the {110} family– (left) and multislip –{112}-type MRSS plane– (right) conditions are shown. The yellow shaded area marks the region where the dislocation velocity is not fast enough to activate slip, v<v^* (see text).

where for simplicity we have replaced $\Theta(\boldsymbol{\sigma})$ in eq. (2.2) with the ratio τ_{RSS}/σ_P. Solving for $\tau = \tau_f$ when v=v^* leads to:

$$\tau_f = \sigma_P \left[1 - \left[\frac{kT}{\Delta H_0} \log\left(\frac{\nu_0 h(L-w)}{v^* b}\right)\right]^{\frac{1}{q}}\right]^{\frac{1}{p}} \tag{2.12}$$

The above equation can be reduced to an expression of the type:

$$\tau_f = \sigma_P \left(1 - (b_3 T)^{\frac{1}{q}}\right)^{\frac{1}{p}} \tag{2.13}$$

where the constant $b_3 = \frac{k}{\Delta H_0} \log\left(\frac{\nu_0 h(L-w)}{v^* b}\right)$ takes a value of 1.55×10^{-3} K^{-1} for $L = 400b$ and the parameters given in Table 2.1. Equation (2.13) is plotted as a contour map in Figure 2.7. The inset to the figure shows the temperature variation of τ_f for L=$400b$ (marked

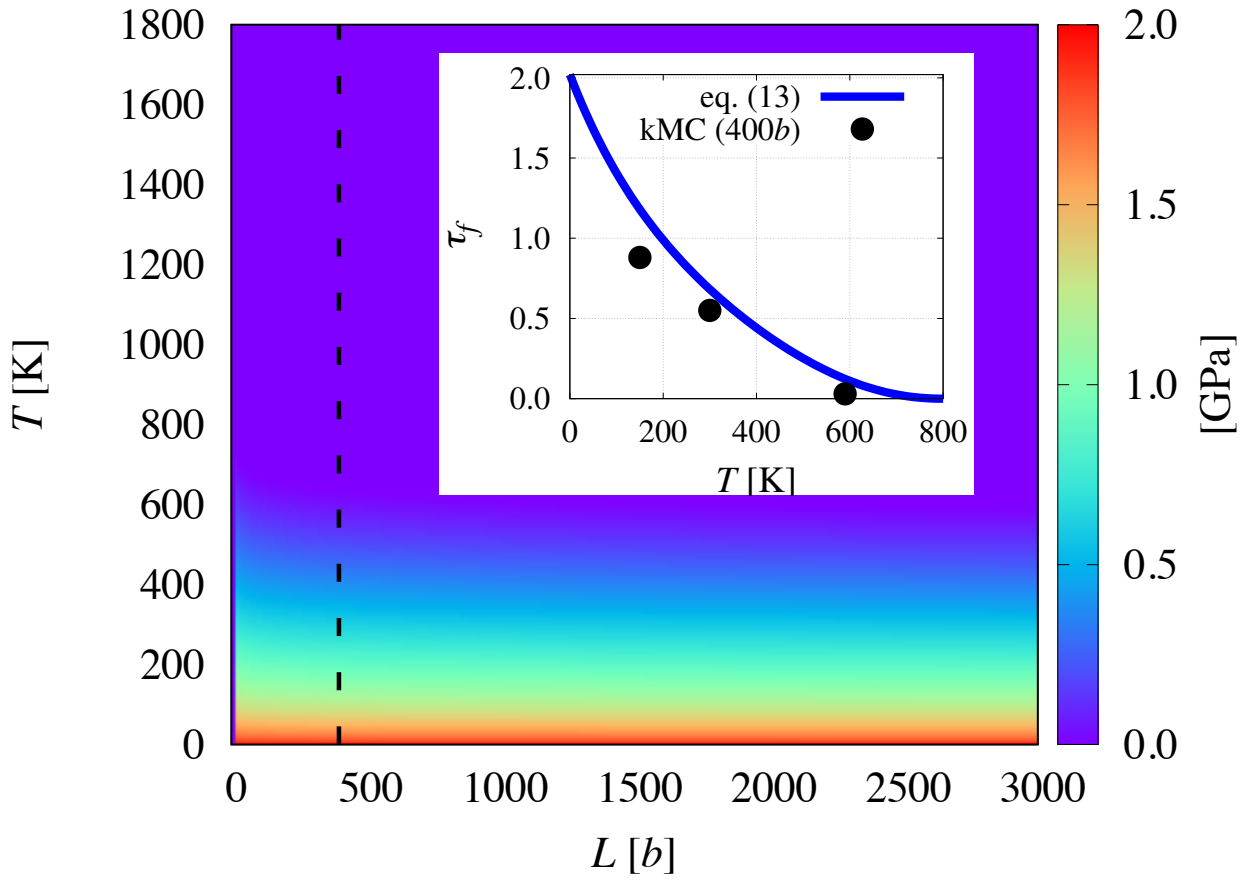

Figure 2.7: Contour map of the flow stress τ_f as a function of dislocation length L and temperature T according to eq. (2.13). The inset shows τ_f at L=400b (marked with a dashed line in the contour plot), as well as the three points obtained from the intercepts for 0% Re in Fig. 2.6.

with a dashed line in the main plot). More importantly, the three points obtained via kMC simulations in Fig. 2.6 for 0% Re are also plotted to confirm the consistency between the analytical and numerical approaches[1]. Next, we calculate τ_f as a function of c and T following the intercept technique discussed above.

The numerical results for τ_f as a function of Re content at 300 K under single slip conditions are shown in Figure 2.8, with the minimum at c=1.5%. The general dependence on temperature is shown in Figure 2.9. All curves show a region of softening at low solute

[1]The disagreement can be attributed to the absence of non-Schmid stresses in the analytical approach, and the stochastic variability of the kMC simulations.

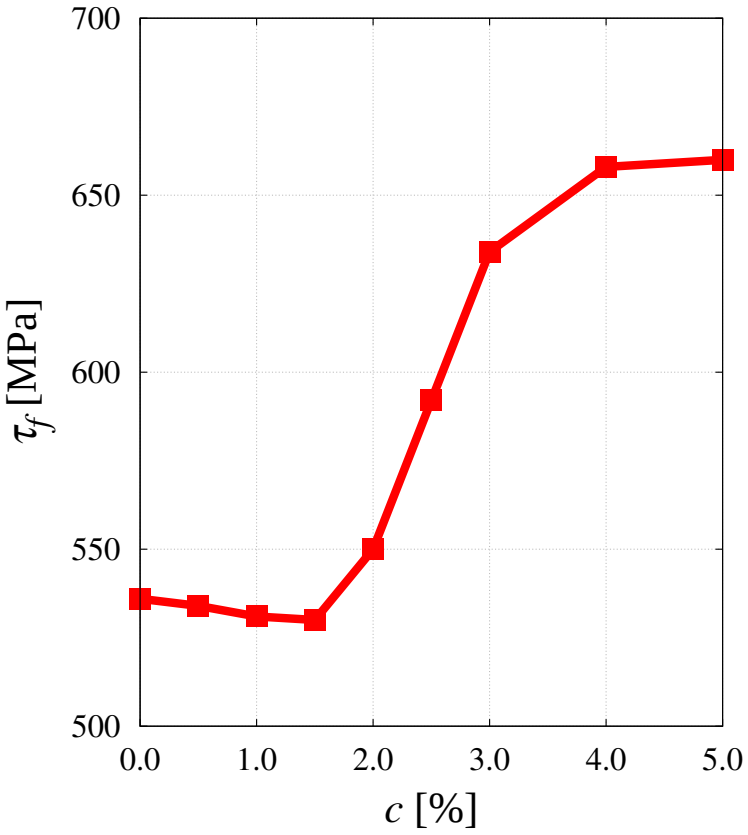

Figure 2.8: Flow stress variation with Re concentration at 300 K under {110} loading conditions.

concentrations, with a gradual transition to a hardening regime at higher values of c. The experimental data by Stephens [130] are shown in the figure for comparison. As shown, the agreement with the measurements increases with temperature although it must be noted that the experimental data were obtained from full stress-strain curves, while our definition of τ_f is for a system with just one dislocation. The location of the minima at each temperature can be plotted into a phase diagram that delineates the separation of the softening and hardening regimes. This is seen in Figure 2.10, which can be considered a preliminary design map. We do not expect a strong dependence of the transition stress on dislocation line length in the laminar slip regime (only one kink-pair at a time on the dislocation), and so these results are in principle extrapolable to systems with higher dislocation densities such as W-Re in the cold-worked state.

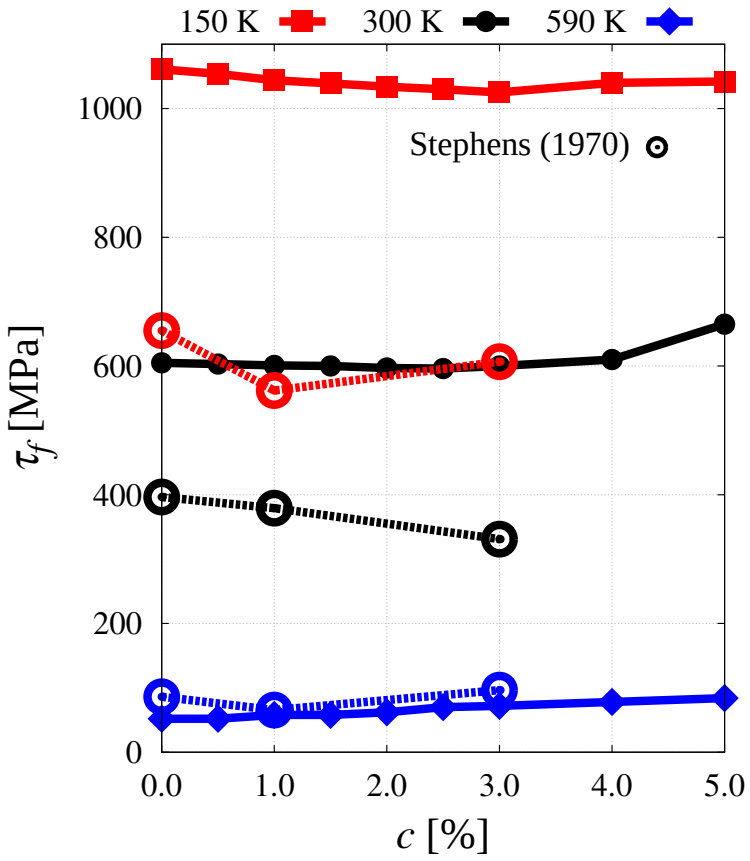

Figure 2.9: Dependence of the flow stress on Re concentration and temperature. The experimental measurements by Stephens are given for comparison [130].

2.4 Discussion

The main purpose of this work is to assemble a computational model that incorporates the main physical mechanisms of substitutional solute-screw dislocation interactions in a bcc alloy. The motivation for the development of the model was to test the applicability limits of the softening effect of Re solute atoms on the Peierls stress of screw dislocations in W-Re, which is a general phenomenon known to occur in most bcc metals [138]. This limit manifests itself as a minimum in the yield/flow stress-concentration curve, which is known to cause shifts in the DBTT compared to pure W. Characterizing this transition from solid solution softening to solute hardening in substitutional bcc alloys has been the subject of much discussion in the literature [42, 66, 75, 94, 100, 107, 108]. It is generally well

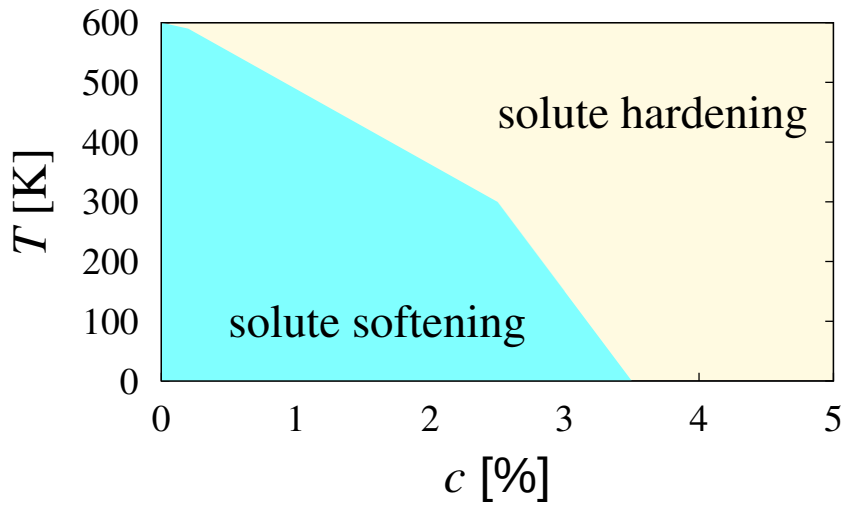

Figure 2.10: Solute softening/hardening map as a function of temperature and concentration under multislip conditions.

accepted that, before the minimum, the presumed softening of the Peierls stress with solute content aids kink-pair nucleation while having a negligible impact on kink-pair propagation. Above the minimum concentration, however, nucleation cannot compensate for the continued interference of solute atoms on kink motion. While there have been early semi-analytical models that build on this idea to predict the transition temperature and solute content, they have been mostly phenomenological due to a lack of understanding of the atomic-scale mechanisms involving dislocation cores and solute atoms. For example, Sato *et al.* [121] were among the first to develop models to explain the transition in terms of the motion of a screw dislocation through a Peierls potential dotted with misfit strain centers representiing solute atoms. As well, there are more recent studies that also capitalize on these basic phenomenological premises [51, 58]. Here, not unlike the work by Sato *et al.*, we develop a model based on the motion of a screw dislocation line through a solid solution. What separates our model from other approaches is the consideration of two of the most critical features of screw dislocation glide in bcc metals: thermally-activated kink-pair nucleation and non-Schmid effects. We have spent a great deal of time quantitatively characterizing these two [20, 102, 133], as well as the solute-dislocation interaction energetics for W-Re from first-principles calculations [49, 114]. This has opened up the possibility to perform *predictive*

simulations, which is what we report in this paper.

Our method has two restrictions that are worth noting. First, it is limited to a single dislocation, which ignores potential interactions with other dislocations and collective dislocation effects. However, there is now a growing consensus that the plastic response of most bcc metals and alloys can be characterized in terms of single-screw dislocation properties [**?**,**?**,**?**]. This is particularly true at low homologous temperatures, where the temperature dependence of the flow stress is particularly pronounced and edge dislocations play no discernible role on plastic flow. It is worth mentioning that experiments have shown that Re additions to tungsten promote the formation of edge dipoles at temperatures which are otherwise too low to hold any significant edge dislocation populations [130], e.g. 300 and 150 K, and increase dislocation density at all temperatures. While this may change the global balance of dislocation subpopulations, we believe that the softening-to-hardening transition is still controlled by local dislocation-solute interactions, well captured in this model. Second, our framework admits only {110} slip[2], while it has been postulated that {112} slip may represent the primary slip plane at higher temperatures. While this has not been conclusively established [10, 83, 123], we have shown in prior works that the temperature dependence of the flow stress in single crystal W can be explained resorting solely to {110} slip [20]. Indeed, the results reported here show that the transition can be captured considering {110} glide only. It has been claimed that rhenium can increase the likelihood of slip on multiple {110} planes, even when the MRSS plane itself belongs to the {110} family. We have conducted analyses of the dislocation core trajectories as a function of concentration and have not found significant differences between pure W and W-Re[3]. In any case, we take our method to be strictly valid in the lower (homologous) temperature region of the flow stress curve, which is the regime considered here.

Finally, this work follows the line of research initiated by Cai and Bulatov [14, 15] and Deo and Srolovitz [27, 29], where the foundations for the current model were laid. Extension

[2]That is, kink pairs can only form on {110} planes, regardless of the MRSS plane.

[3]Instead, temperature is found to have a more pronounced impact on trajectory.

of the current methodology to interstitial solutes and the study of dynamic strain aging is being currently pursued.

CHAPTER 3

Electronic structure calculations of oxygen atom transport energetics in the presence of screw dislocations in tungsten

3.1 Introduction

Refractory transition metals such as those in groups V and VI of the periodic table belong to a class of materials with important potential applications thanks to their high-temperature strength and corrosion resistance [25, 64, 136]. However, they typically display poor low-temperature fracture toughness and must be alloyed with other transition metal elements to improve their ductility. For example, in the case of body-centered cubic (bcc) W, W-Re alloys have been shown to lower the ductile-to-brittle transition temperature by up to hundreds of degrees [63], resulting in commercially viable alloys. Interstitial impurities, however, are known to produce marked increases in the ductile-to-brittle transition temperature of polycrystalline specimens [129]. Specifically, oxygen is seen to lower both the tensile and yield strengths, while promoting intergranular fracture at concentrations as low as 30 appm. In single crystals, the effect is less pronounced, although some evidence suggests a hardening effect at low temperatures [126,127,140]. As well, oxygen is known to be involved in dynamic strain aging in tungsten-based alloys deformed within a certain strain rate and temperature window [4,24]. In principle, O is soluble in tungsten up to the formation of the line compound WO_2 at 66.7 at.% [152], although embrittling second phases have been seen to form at grain boundaries at only a few appm of concentration [128]. In single crystals, the effect can be isolated to dislocation core/solute interactions, particularly screw dislocations, as they are

known to control plasticity in bcc metals at low-to-intermediate temperatures [21, 23, 148]. By its very nature, this interaction can only be studied using atomistic resolution methods to describe the large deformations found around the dislocation core. At the same time, the method must capture the essential details of W-O chemistry, which may become important in non-dilute conditions. These restrictions point to density functional theory (DFT) as the technique of choice to investigate dislocation-O interactions in W.

Numerous studies have been performed on dislocation core/solute interactions using DFT calculations. For substitutional solutes, several works including face and body-centered materials exist [53, 69, 87, 113, 114, 119, 139, 159], while for interstitial impurities several calculations including a number of different solutes in Fe have been recently published [77, 112, 145], as well as dislocation-C interactions in most bcc transition metals [76]. These calculations show that solute atoms stabilize the hard core configuration of a screw dislocation when the solutes are placed inside the triangular prism formed by the the three $\langle 111 \rangle$ atomic rows enclosing the dislocation core.

Interestingly, despite its technological importance, no DFT studies have been performed on the interactions between dislocation and O in W. The primary objective of this work is to investigate the interactions of oxygen interstitial solute with screw dislocations in bcc W. These interactions can be categorized as *long-range*, i.e. elastic interactions affecting the diffusive behavior of oxygen atoms in the presence of dislocations, or *short-range*, i.e. local binding of chemical nature between dislocation cores and impurities. Consequently, here we study first the dependence on stress of the diffusivity of O interstitials atoms in bulk W, followed by the calculation of interaction energies between O atoms and screw dislocation cores. We end the paper with a discussion and the conclusions.

3.2 Computational details

All DFT calculations were carried out using the Vienna Ab Initio Simulation Package (VASP) code [60] and the *projector augmented wave* (PAW) [8,61] pseudopotential scheme within the

Perdew-Burke-Ernzerhof (PBE) generalized gradient approximation and a 400 eV kinetic-energy cutoff. The Hermite-Gaussian scheme was employed, with a smearing of 0.2 eV for electronic occupation. Structure relaxation was performed until the forces on all the atoms were less than 2×10^{-2} eV/Å.

3.2.1 O solution and migration energies under strain

Calculations of O-atom solution and migration energy in bulk W were performed using 250 atoms bcc supercells with a 4×4×4 k-point grid. The migration barrier was calculated between two neighboring configurations of lowest energy (tetrahedral sites in the present case) using the *nudged elastic band* (NEB) method as implemented in VASP. O migration in bulk W under strain was investigated by applying the following transformation matrices to the supercell lattice vectors:

$$\vec{a}' = (\boldsymbol{\varepsilon} + \boldsymbol{I})\,\vec{a} \tag{3.1}$$

where $\vec{a}'$ are the deformed lattice vectors, $\boldsymbol{\varepsilon}$ is the applied strain tensor, $\boldsymbol{I}$ is the identity tensor, and $\vec{a}$ are the undeformed lattice vectors. The undeformed configuration is expressed in a canonical cartesian reference system with $\vec{a_1} \equiv [a_0\ 0\ 0]$, $\vec{a_2} =\equiv [0\ a_0\ 0]$, and $\vec{a_3} \equiv [0\ 0\ a_0]$, where $a_0 = 3.186$ Å is the lattice parameter of W calculated with the pseudopotential employed here. Two different strain tensors were applied for the simulations:

(i) Hydrostatic strain:

$$\boldsymbol{\varepsilon} = \begin{bmatrix} \epsilon & 0 & 0 \\ 0 & \epsilon & 0 \\ 0 & 0 & \epsilon \end{bmatrix}$$

(ii) Volume-conserving shear:

$$\boldsymbol{\varepsilon} = \begin{bmatrix} 0 & \gamma/2 & 0 \\ \gamma/2 & 0 & 0 \\ 0 & 0 & 0 \end{bmatrix}$$

where ϵ and γ are the applied dilatational and shear strains, respectively. Positive values of ϵ are taken to represent tensile distortions. Note that in the limit of small deformations, (i)

the volumetric strain $\varepsilon_v = \Delta V/V \approx \boldsymbol{Tr}(\boldsymbol{\varepsilon}) = 3\epsilon$, and (ii) $\gamma = \tan\theta$, with θ the shear angle as defined in Figure 3.1. Note that shear deformation turns a symmetric cubic cell into a monoclinic one, which results in a shortening of certain tetrahedral→tetrahedral paths and in extension of others, as illustrated in the figure. This is equivalent to applying negative shear strain and, consequently, we have investigated both reaction paths when calculating O migration in sheared bcc W. We used 10 NEB images in the majority of the cases considered here, the only exceptions being $\epsilon = 1\%,\ 2\%$ and $\gamma = 1\%$, where 7 images where used.

3.2.2 Screw dislocation-O interaction

Simulations of dislocation-O interactions were performed using 135 W-atom supercells containing two screw dislocation cores with Burgers vectors $+\vec{b}$ and $-\vec{b}$ ($\vec{b} = {}^{a_0}/_2[111]$) arranged in a balanced quadrupolar configuration, as is typically used for such simulations [22,32,144], with a 1×2×16 k-point grid. The cell was first relaxed in the absence of oxygen to determine the reference configuration for dislocation-solute interactions. This results in a non-degenerate, *easy* core configuration, consistent with a number of other independent DFT calculations [32, 50, 52, 143, 144, 151]. Solute atoms were subsequently placed at various tetrahedral sites around both dislocation cores to ensure symmetric structures with equivalent energies. Figure 3.2 represents an expanded view of one of the dislocation cores of the supercell in order to highlight the six tetrahedral sites investigated as initial positions of the O atom. A differential displacement map is used to identify the position of the dislocation in the figure [33, 147]. The use of periodic boundary conditions along the [111] direction when placing an O atom in the supercell results in a row of atoms separated by a distance of $1b$ (equal to the thickness of the box). We tested the impact of using such thin specimens by repeating one of the calculations with a thickness of $2b$ to preliminarily quantify the box thickness effect on the final results.

3.3 Results

3.3.1 Oxygen atom stability in bulk tungsten

Oxygen stability in bulk W is evaluated by separately inserting one oxygen atom in tetrahedral and octahedral sites of a bulk W bcc structure. Figure 3.3 shows the geometric location of the interstices in a bcc unit cell. The solution energy H_s (heat of solution) is defined as:

$$H_s = E_{\text{W-}O} - E_{\text{W}} - \mu_{\text{O}} \tag{3.2}$$

where $E_{\text{W-}O}$ and E_W are, respectively, the energies of a W cell with and without O, and μ_{O} is the reference energy of a single O atom (chemical potential). In accordance with previous works [53,56], we take μ_{O} to be half of the total energy of a O_2 molecule, which is calculated to be -4.92 eV (compared to -1.59 eV for an isolated O atom in a vacuum), i.e.:

$$\mu_{\text{O}} = \frac{1}{2}E_{\text{O}_2} = -4.92 \text{ e}V$$

With this, we find a solution energies of 1.01 eV and 0.70 eV for for octahedral and tetrahedral sites, respectively. While this is consistent with recent studies in W-O [1,91], it deviates from what is found in other bcc metals, where octahedral sites are more stable for interstitial impurities[1] [77, 78]. The reasons behind this behavior appear to be related to the overlap between the electron charge densities of O and W when the O atom is at a tetrahedral location [1].

Next, we study the dependence of H_s with strain applied in the manner described in Sec. 3.2.1. The results are shown in Figure 3.4, clearly indicating a strong coupling to volumetric strain but an almost negligible one to shear deformation. Assuming a linear dependence with ϵ, we find:

$$H_s(\epsilon) = 0.70 - 57.7\epsilon = 0.70 - \frac{57.7p}{3B_{\text{W}}} \; [eV]$$

[1]Consistent with an octahedral volume of $V_{oct} = a_0^3/3$, versus a tetrahedral one of $V_{tet} = a_0^3/12$.

where $p = {}^1/_3\boldsymbol{Tr}(\boldsymbol{\sigma})$ is the pressure, B_{W} is the bulk modulus of pure W. For a value of $B_{\mathrm{W}} = 308.5$ GPa calculated using the same pseudopotential, we obtain the dependence of the heat of solution with stress:

$$H_s(\boldsymbol{\sigma}) = 0.70 - 9.98 \times 10^{-3} p = -0.70 - 3.33 \times 10^{-3}(\sigma_{xx} + \sigma_{yy} + \sigma_{zz}) \; [eV] \tag{3.3}$$

with p and the components of $\boldsymbol{\sigma}$ expressed in MPa.

We have also calculated the formation energy of an O atom at a vacant site and have obtained a value of -0.14 eV. This association with a vacancy results in a *substitutional* O atom, which, as earlier DFT calculations have shown for other interstitial solutes [6], effectively immobilizes it, thus changing the character of its contribution to the kinetic evolution of the system. This case will not studied further and in the following we focus on interstitial oxygen migration pathways.

3.3.2 Oxygen migration in bulk tungsten

The migration barrier, E_m, between two neighboring tetrahedral sites was evaluated using the NEB method (refer to Sec. 3.2). For zero strain we find a value of 0.20 eV for the migration energy of O in W, in good agreement with the 0.17 eV obtained by Alkhamees *et al.* [1] and in contrast with values over 0.3 eV for octahedral→octahedral transitions by the same authors. This is also in concordance with both DFT and semi-empirical interatomic potential calculations of O migration in other bcc metals that consistently yield larger values for the octahedral→octahedral jump [38, 39, 71, 124]. Here, we expand on the calculations by Alkhamees *et al.* by studying the dependence of the migration barrier on hydrostatic and shear strain. Results for tensile and compressive strains are shown in Figure 3.5a. The results reveal a linear dependence of the migration energy barrier on hydrostatic strain, as shown in Fig. 3.5b, with a proportionality constant of $k_{hydro} = 2.74$ eV. This implies a constant activation volume, which for this transition can be calculated as:

$$\Omega_{hydro} = \frac{k_{hydro}}{3B_{\mathrm{W}}}$$

For the value of B_{W} given above, $\Omega_{hydro} = 0.47$ Å$^3 = 0.022b^3$.

The dependence of the migration energy on shear strain is shown in Figure 3.6a. As mentioned above, shortened and lengthened paths (refer to Fig. 3.1) are simply manifestations of the sign of the applied shear strain and thus we show all the calculations on the same plot. In the case of shear, the activation volume is defined as:

$$\Omega_{shear} = \frac{k_{shear}}{\mu_{\mathrm{W}}}$$

where, from the results in Fig. 3.6b, $k_{shear} = 3.70$ eV is the proportionality constant and $\mu_{\mathrm{W}} = 160.2$ GPa is the shear modulus for the current pseudopotential. With this, an activation volume $\Omega_{shear} = 3.98$ Å$^3 = 0.19b^3$ is obtained.

It is worth noting that although the reaction path in Figs. 3.5a and 3.6a is shown as projected along the rectilinear path joining two first-nearest neighbor (NN) tetrahedral sites, the actual trajectory is curved, as can be seen in Figure 3.7 for the unstrained case. The figure also shows the positions of two octahedral sites lying on the same (001) plane as the tetrahedral ones. It is important to point out that the while the octahedral position represents a local minimum for the O atom, the saddle point of the tetrahedral→tetrahedral transition is still a lower energy state than the octahedral one. This strengthens our assumption to discard octahedral→octahedral transitions as energetically less relevant than their tetrahedral→tetrahedral counterparts.

3.3.3 Screw dislocation-oxygen interaction in tungsten

The calculations carried out in the previous section allow us to couple solute diffusion to the dislocation elastic fields. However, there also exists an *inelastic* interaction that takes place when the solute atom is found close to the dislocation core. There, local nonlinear effects dominate over long-range elastic interactions and it is therefore important to quantify them. Next we calculate the interaction energies between oxygen atoms and screw dislocation cores in W using the geometries described in Sec. 3.2.2. The interaction energy is defined as:

$$E_{\mathrm{i}} = \frac{1}{2}\left(E^{dislo}_{\mathrm{W}\text{-}O} - E^{dislo}_{\mathrm{W}}\right) + \left(E^{bulk}_{\mathrm{W}} - E^{bulk}_{\mathrm{W}\text{-}O}\right) \tag{3.4}$$

where $E^{dislo}_{\text{W-}O}$ and E^{dislo}_{W} are the energies of the dislocated cells with and without oxygen atoms, respectively, while $E^{bulk}_{\text{W-}O}$ and E^{bulk}_{W} are the energies of bulk W with and without O atoms. The $1/2$ factor is used to account for the existence of two dislocations in the simulation cell with their corresponding oxygen atoms located at one of the six nearest tetrahedral sites to the dislocation core, as illustrated in Figure 3.2. Upon relaxation of the dislocation-O system in W, we find that only two stable final configurations are possible, depending on the initial position of the O atom, as illustrated in Figure 3.8. In the figure, the initial positions of the dislocation cores and the oxygen atoms are marked with blue crosses and blue circles, respectively, while their final relaxed positions are shown using red crosses and filled red dots. As for the reference configuration, differential displacement maps are used to identify the position of dislocation cores after relaxation.

Figure 3.8a shows the final configuration for the case where the O atom was originally introduced in the 4^{th} NN position. One can see that upon relaxation the dislocation core remains compact and symmetric, but its center has shifted towards the center of a neighboring downward-pointing triangle. This final dislocation core configuration corresponds to the so-called *hard* core configuration. Although the hard core configuration is known to be unstable in W and in most pure bcc metals [32, 76], here we find that the presence of O induces a reconstruction from the easy to the hard core configuration, similar to what has been reported for W-C in refs. [76, 146]. Because of this shift after relaxation, the relative position of the oxygen atom changes from 4^{th} NN to 2^{nd} NN. Indeed, this was found to be the case for initial O atoms positions located in 1^{st}, 2^{nd}, 4^{th} and 6^{th} NN tetrahedral sites, all with an interaction energy of -1.83 eV, which is indicative of a strong short-range interaction between the dislocation core and the oxygen atom.

A second possible stable configuration was obtained by relaxation of the dislocation-O system when the oxygen atom was inserted in the 5^{th} NN tetrahedral site. In that case, both the dislocation cores and the O atoms remain in their initial positions, as illustrated in Figure 3.8b by the superposition of blue and red crosses and points that indicate the initial and final dislocation and O positions. The final core configuration is a distorted easy

core, where the core is seen to spread between its original location and that of the O atom. A similar configuration has been reported for C interstitials in Ta [76]. Thus, the 5^{th} NN tetrahedral site appears to be a second stable possibility for the O atom in the vicinity of the dislocation core, with a corresponding interaction energy of -1.20 eV. Finally, when O is initially located in the 3^{rd} NN tetrahedral site, one of the dislocations of the dipole shifts to a hard core configuration with the O atom in the 2^{nd} NN position, and the other relaxes to the distorted easy core of the 5^{th} NN configuration. Not surprisingly its interaction energy is -1.52 eV, which is exactly the average of the energies of the 2^{nd} and 5^{th} NN cases.

All the calculated energies are strongly negative, indicating a strong attraction between O atoms and the dislocation core. This is consistent with calculated elastic distortions of near 40% in the atoms bounding the tetrahedral site around the solute atom (analyzed using local atomic displacements in OVITO [132]). The effect of the dislocation core is thus to accommodate these distortions caused by the O atom into its own displacement field, resulting in energetically very favorable configurations. For its part, it is seen that the deformation field due to the solute decays very rapidly, such that it is almost zero at second nearest neighbor positions from it.

3.4 Discussion

The present calculations are intended to provide quantitative support for mesoscale models of dislocation-solute coevolution, ultimately designed to explore the mechanisms behind serrated flow in bcc metals. As such, two types of interactions must be characterized, long and short range, of elastic and inelastic nature, respectively. The former affects tetrahedral→tetrahedral oxygen atom migration under dislocation stress fields via an Arrhenius expression of the following type:

$$\nu\left(T, \boldsymbol{\sigma}(\vec{\boldsymbol{r}})\right) = \nu_0 \exp\left(-\frac{\Delta H_a(\boldsymbol{\sigma}(\vec{r}))}{kT}\right) \tag{3.5}$$

where ν_0 is an attempt frequency, ΔH_a is the *activation* enthalpy for the diffusive jump and k and T are Boltzmann's constant and the absolute temperature, respectively. The activation

enthalpy has several contributions:

$$\Delta H_a = E_m + \Delta H_s - W_m$$

with:

$$E_m = 0.20 \text{ eV}$$
$$\Delta H_s = H_s(\boldsymbol{\sigma}(\vec{r_2})) - H_s(\boldsymbol{\sigma}(\vec{r_1}))$$
$$W_m = \boldsymbol{\sigma}(\vec{r_1}) : \boldsymbol{\Omega}$$

where W_m is the mechanical work and $\boldsymbol{\Omega}$ is the activation volume tensor obtained in this work:

$$\boldsymbol{\Omega} = \frac{\partial E_m}{\partial \vec{\sigma}} = \begin{bmatrix} \Omega_{hydro} & \Omega_{shear} & \Omega_{shear} \\ \Omega_{shear} & \Omega_{hydro} & \Omega_{shear} \\ \Omega_{shear} & \Omega_{shear} & \Omega_{hydro} \end{bmatrix} = b^3 \begin{bmatrix} 0.022 & 0.190 & 0.190 \\ 0.190 & 0.022 & 0.190 \\ 0.190 & 0.190 & 0.022 \end{bmatrix} \tag{3.6}$$

In eq. (3.5), $\boldsymbol{\sigma}$ represents the stress tensor defined at spatial points $\vec{r_1}$ and $\vec{r_2}$ representing the initial and final coordinates of the O atom transition, including all contributions, e.g. applied external stress, stresses from other dislocation segments, etc.

Our computed energies can also be put in the context of experimental measurements of oxygen diffusion in W. There were a number of studies looking at diffusion profiles of oxygen atoms in exposed W surfaces performed in the 1960s [54, 65, 106], and more recently in oxidized W specimens [13, 125]. In general, activation energies between 1.0 and 2.0 eV are found in these tests. Our calculations (activation energy: $H_s + E_m \approx 0.9$ eV) fall in the low end of these measurements. However, it is difficult to separate the effects due to surface roughness, impurity content, and other imponderables, from the experiments, while our calculations of course are free from these.

For its part, the inelastic effect occurs locally at the dislocation core, where linear elasticity is no longer suitable to capture the dislocation-oxygen interaction. A strong dislocation core-O atom attraction is found, as evidenced by interaction energies of up to 1.83 eV. While this is generally consistent with existing DFT studies of small interstitial impurities bound to screw dislocation cores in the literature [5, 73, 76, 77, 146] it must also be kept in mind that

the present calculations are done for dislocation segments of length $1b$, and thus a contribution to E_i from periodic image O-O interactions cannot be discounted. By way of example, the interaction energies found in cells with thicknesses of $1b$ and $2b$ were -1.83 and -1.60 eV respectively, for the case of a 2^{nd} NN stable O position. This suggests that a portion of the interaction energy calculated here is attributable to the stabilization effect created by the O-O bond. By way of example, we have calculated a relaxed bond length in the O_2 molecule of 1.23 Å, in good agreement with prior works [149, 158]. While still smaller than the cell thickness of $b = 2.75$ Å, it appears to have a measurable impact on the final interaction energies. To ascertain this in more quantitative terms, we have also calculated the energy of a O-O pair separated by distances of $1b$ and $2b$. The results are given in Table 3.1:

Table 3.1: Bond lengths, total and half energies of O-O complexes in the vacuum. The top row corresponds to the stable O_2 molecule.

$d_{O\text{-}O}$[Å]	$E_{O\text{-}O}$ [eV]	$1/2E_{O\text{-}O}$ [eV]
1.23 (O_2)	-9.84	-4.92
2.76 ($1b$)	-3.74	-1.87
5.52 ($2b$)	-3.18	-1.59

We recall that the energy of an isolated O atom is -1.59 eV (Sec. 3.3.1), which means that at a separation of $2b$ an O-O pair can be regarded as a pair of isolated atoms. This implies that computational cells with thicknesses of $2b$ are sufficient to eliminate any O-O bonding from the simulations along the dislocation line. For separations of $1b$, an O-O pair has a binding energy of -0.56 eV. This is consistent with an excess energy of approximately 0.23 eV between the values of E_i for $1b$ and $2b$ just discussed. In any case, these corrections do not affect our overall conclusions that a high attractive energy is governs solute-dislocation core interactions, based on which it is reasonable to assume that the inelastic effect dominate over the elastic one as it relates to long-term evolution.

Additionally, when O atoms decorate the dislocation line in the manner created by the DFT calculations presented here, the core structure is seen to stabilize in preferentially in

a 'hard' core configuration. Whether this is the case for longer dislocation segments (>2b), i.e. for smaller O-atom linear densities, is not clear at present. On this point, it is worth noting that, although the hard core is in general a higher energy configuration for screw dislocations in bcc metals [32,52,144,155], several studies have shown that it can be stabilized by both substitutional [119, 145] and interstitial [77, 146] solute atoms, in agreement with the present study.

All the above effects must be included in simulations of microstructural evolution to study the fundamental mechanisms behind interstitial solid solution softening/hardening or dynamic strain aging. We have some experience developing this type of models for substitutional alloys [161], which allow us to push the length and timescale envelope to experimentally-meaningful levels. The coupling of the energetics obtained in this work and mesoscopic models of dislocation-solute evolution is the subject of an ongoing effort which will be published in future studies.

3.5 Conclusions

- We have conducted electronic structure calculations of the fundamental energetics of oxygen atoms in tungsten, including the heat of solution, migration energies, activation volumes, and interaction energy with screw dislocation cores.

- Oxygen atoms are preferentially found in tetrahedral lattice sites, with solution energies of 0.70 eV. The *substitutional* heat of solution (an O atom associated with a vacant site) was found to be −0.14 eV.

- The migration energy for the tetrahedral→tetrahedral transition in the bulk is 0.20 eV. This energy is modified by stress according to activation volumes of $0.02b^3$ and $0.19b^3$ for volumetric and shear deformations, respectively.

- The interaction energy between a screw dislocation core and an O atom depends on the relative position of the oxygen but it is found to be either 1.20 or 1.83 eV, depending

on the final configuration. We find that this is due to the accommodation of the large local distortions induced by the O atom in the lattice, which is seen to lead to a core reconstruction from an easy core configuration to a hard core one when O atoms are present.

- In most cases, once absorbed at a screw dislocation core, O atoms are seen to induce a dislocation core transformation from an easy core configuration to a hard core one.
- These calculations will serve to parameterize mesoscale models of material deformation by dislocation slip.

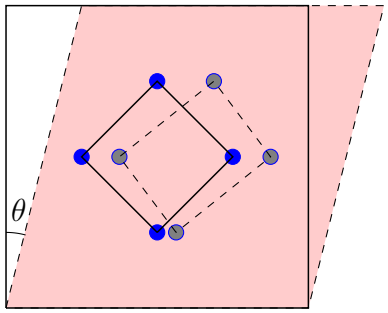

Figure 3.1: Illustration of the distortion of tetrahedral→tetrahedral paths under shear deformation. The undeformed path becomes stretched along two directions and compressed along the other two. θ represents the shear angle (refer to Sec. 3.2).

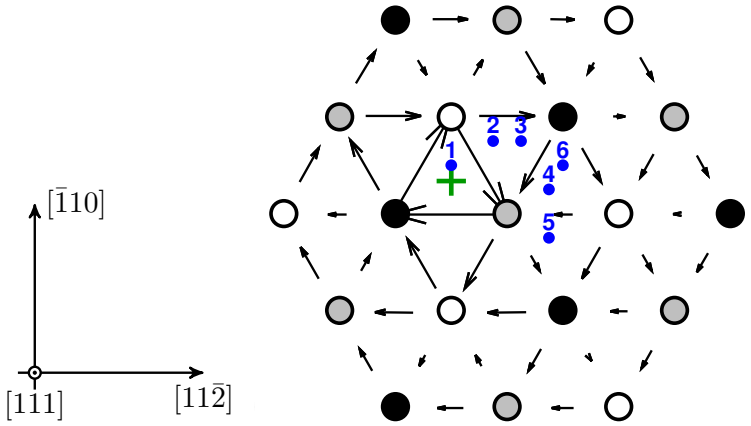

Figure 3.2: Location of the six nearest tetrahedral sites (blue points) to the geometric center of a screw dislocation core (green cross) before the relaxation of the dislocation-O system with DFT. The dislocation is in an easy core configuration. The arrows represent the amplitude of differential atomic displacements along the $\langle 111 \rangle$ direction (normal to the image) induced by the presence of the dislocation.

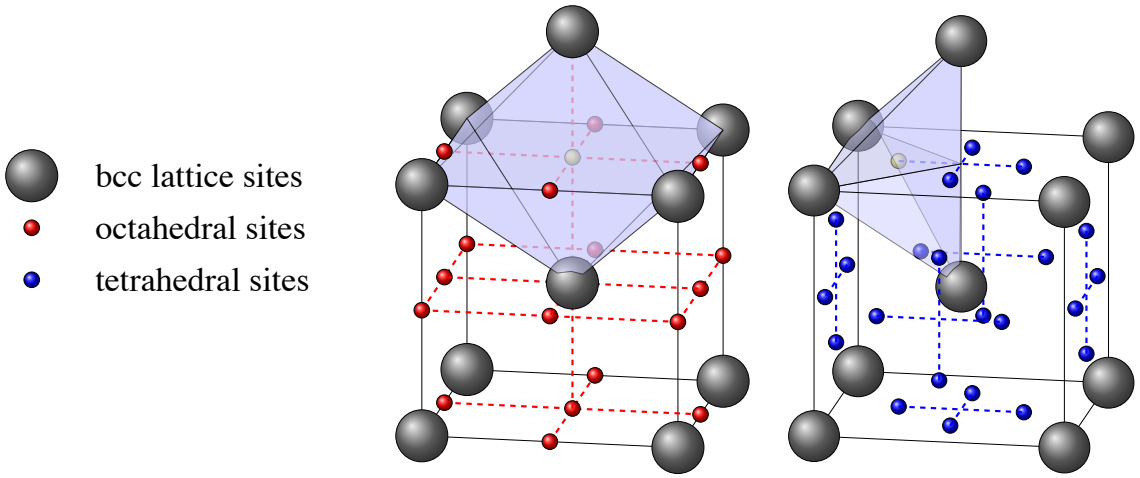

Figure 3.3: Elementary bcc lattice cell showing octahedral and tetrahedral interstitial sites. As a guide to the eye, the figures show a shaded octahedron and tetrahedron with the interstitial site highlighted in their respective centers. In principle, transitions may occur between any two nearest neighbor interstitial sites.

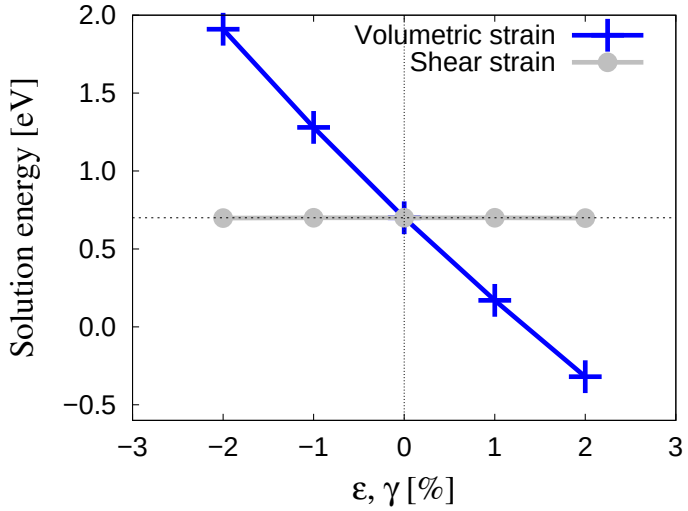

Figure 3.4: Variation of the heat of solution of tetrahedral O as a function of volumetric, ε, and shear, γ, strain.

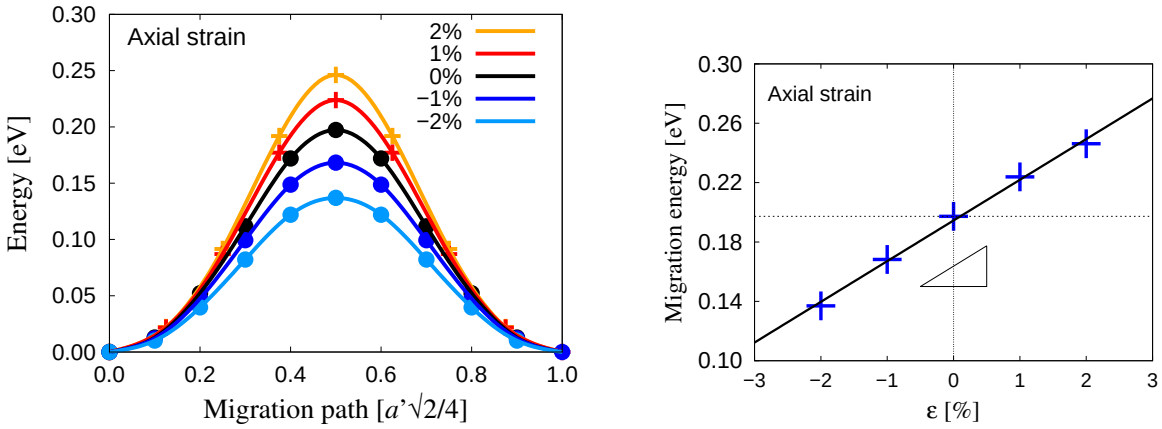

(a) (b)

Figure 3.5: (a) Tetrahedral→tetrahedral oxygen migration energy path in bulk W calculated with DFT between two neighboring tetrahedral sites under hydrostatic strain. a' is defined in eq. (3.1). (b) Migration energy barrier under uniform axial strain. The black line represents a least-squares linear fit, from whose slope (black triangle) the activation volume can be calculated.

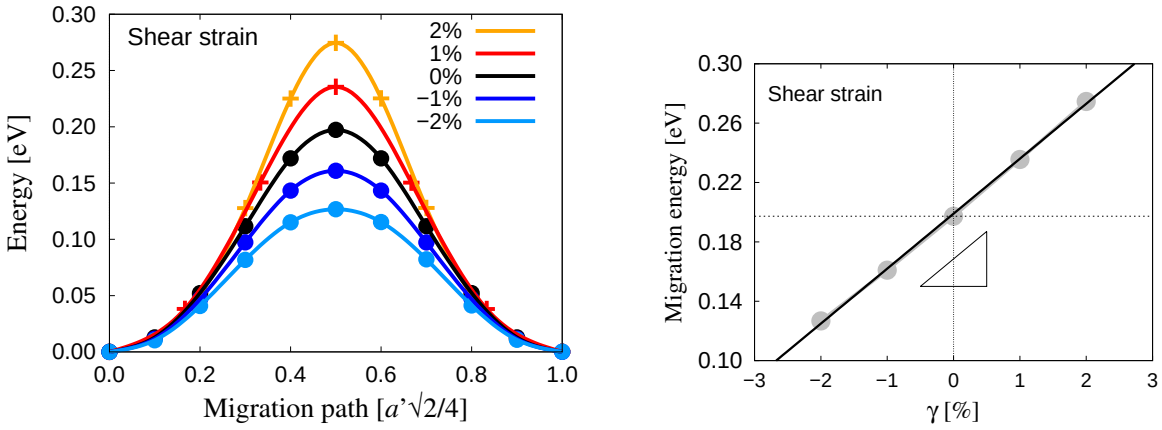

(a) (b)

Figure 3.6: (a) Tetrahedral→tetrahedral oxygen migration energy path in bulk W calculated with DFT between two neighboring tetrahedral sites under shear strain. (b) Migration energy barrier under shear strain. The black line represents a least-squares linear fit, from whose slope (black triangle) the activation volume can be calculated.

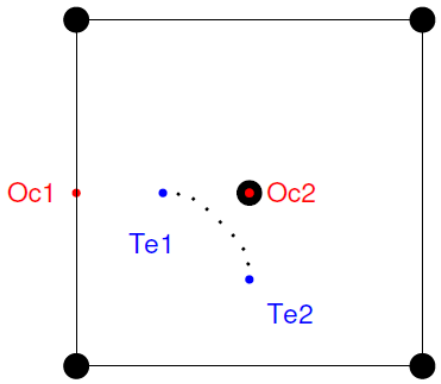

Figure 3.7: Relaxed migration path of an oxygen atom between two tetrahedral sites on a (001) plane under zero strain showing two neighboring octahedral sites for reference. The trajectory follows a curved path arched towards the closest octahedral site.

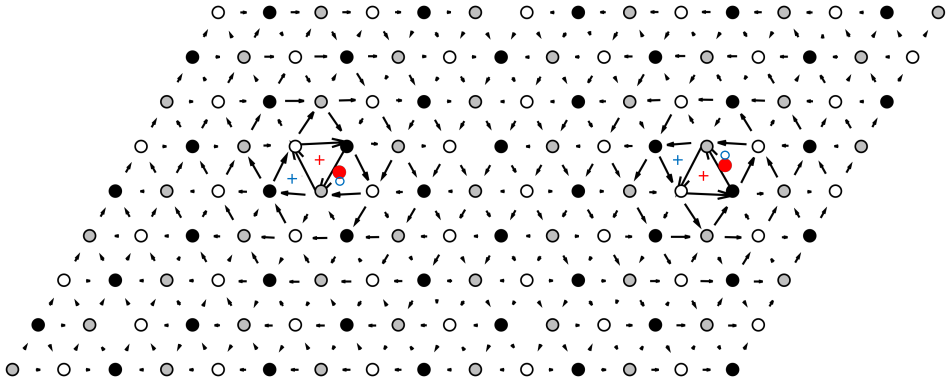

(a) The initial configuration starts with the oxygen atom in a 4^{th} NN tetrahedral position. After relaxation, the core shifts to a hard core configuration and the oxygen atoms shifts to a 2^{nd} NN position. The dislocation maintains its compact core structure after relaxation. The calculated interaction energy is -1.83 eV.

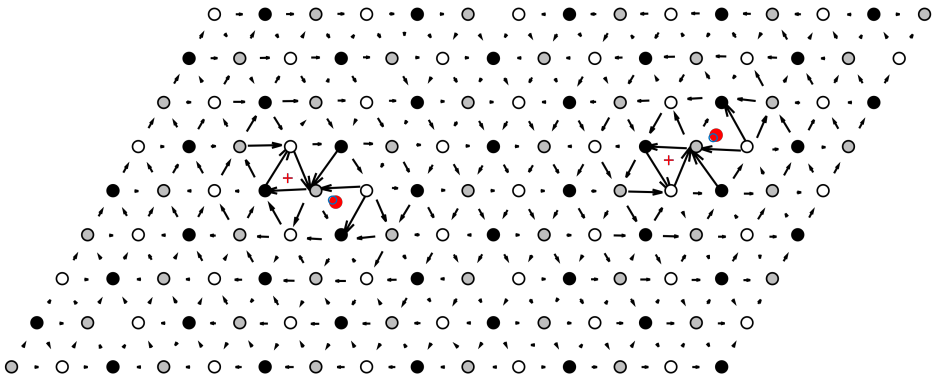

(b) The initial configuration starts with the oxygen atom in a 5^{th} NN tetrahedral position. After relaxation, neither the dislocation or the O atom have shifted, however, the dislocation core becomes asymmetric. The calculated interaction energy is -1.20 eV.

Figure 3.8: Stable relaxed configurations of the dislocation core/O-atom system. All other initial configurations (see Fig. 3.2) relax to one of these. The cross marks the location of the dislocation core (blue: initial, red: final), while the blue and red dots mark the initial and final position of the O atoms, respectively.

CHAPTER 4

Portevin-Le Chatelier effect observed through direct simulations of serrated flow in a body-centered cubic crystal

The Portevin-Le Chatelier (PLC) effect is a well-known phenomenon in materials science by which metallic alloys deform in an unstable manner, potentially leading to poor ductility and premature failure [2, 3, 12, 59, 62, 72, 80, 86, 89, 90, 92, 93, 98, 103, 104, 134, 153, 157]. The PLC effect is characterized by jerky flow and the onset of inhomogeneous deformation, typically attributed to the dynamic interplay between dislocations and solute atoms. The macroscopic manifestation of this process is the appearance of serrated flow in the stress-strain curve, a necessary but not sufficient condition to indicate the existence of dynamic strain aging (DSA). Figure 1 shows stress-strain curves of lath martensite micropillars at room temperature and two different strain rates. The figure exemplifies how changes in strain rate (and/or temperature) can induce drastic variations in the plastic flow of a material. While there are other manifestations of DSA, the most important one is the inversion of the dependence of the strength, σ, on strain rate,$\dot{\epsilon}$, resulting in a negative strain rate sensitivity (defined by an exponent, $m = \Delta\sigma/\Delta \log \dot{\epsilon}$) [99]. The PLC effect belongs to a more general class of unstable phenomena in physics known as intermittent processes. These processes operate in a time-discontinuous manner and are pervasive in the natural world, being found across numerous scientific disciplines [34, 45, 97]. Modeling these processes is challenging both because their intrinsic dynamics are controlled by discrete events (i.e. fluctuations) and because the time and length scales governing fluctuations and the observed macroscopic response are often separated by many orders of magnitude.

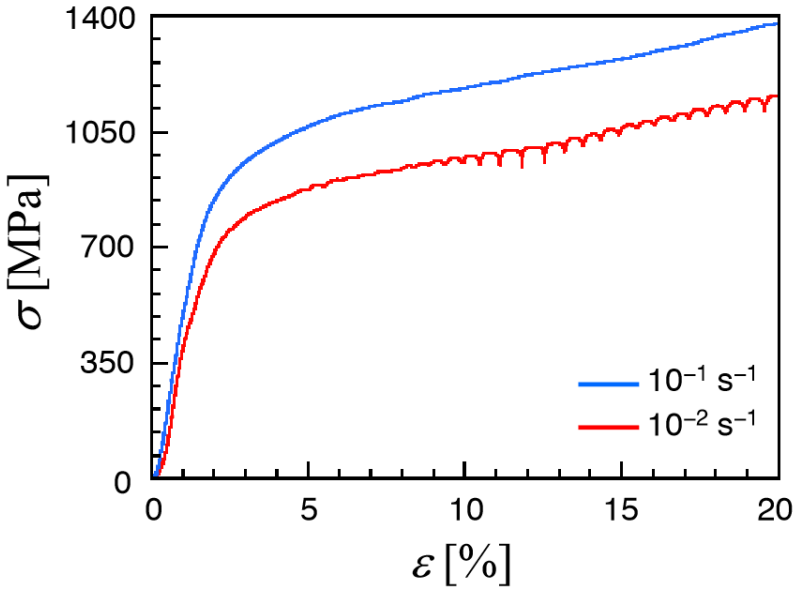

Figure 4.1: Engineering stress-strain curves of lath martensite obtained during in-situ SEM microcompression tests at room temperature for two different strain rates, $\dot{\epsilon}$=10^{-2} ani $\dot{\epsilon} = 10^{-1}$ s^{-1}. Serrated flow is clearly observed during the $10^{-2}s^{-1}$ test (red curve) (See the Methods Section for details on these experiments)

In body-centered cubic (bcc) materials at low-to-moderate homologous temperatures, plastic slip is governed by the motion of screw dislocations on closed-packed planes. Generally, this motion is understood to occur over a periodic energy landscape known as the *Peierls* potential U_P with a periodicity h and an amplitude U_0. At low stresses, slip proceeds via the thermally activated nucleation of steps of height h on the dislocation line, known as *kink pairs*, and their subsequent sideward relaxation. The basic kink-pair geometry and the structure of the potential energy substrate are schematically depicted in Figure 4.2. The occurrence of these kinks makes dislocations in bcc metals behave as a *many-body* system, increasing the complexity of their treatment compared to other materials. Over five decades of research in bcc metals have conclusively revealed a direct connection between the kink pair activation enthalpy and the temperature dependence of the flow stress in all pure bcc metals [16]. In alloys, solutes are known to alter kink-pair nucleation and propagation rates giving rise to several well-known phenomena in bcc plasticity. For example, some substitutional bcc solid solutions are known to suffer a transition from solute *softening* to solute *hardening* as a function of alloy concentration [43,74,101,131]. This is now known to be a direct consequence of the interaction between solutes and kink pairs [17]. Also, substitutional solutes are known to lower the so-called *knee* temperature, after which screw dislocation motion becomes athermal and the mobility of screw and non-screw segments becomes comparable [135]. Owing to their low diffusion rates and the absence of a vacancy-generation mechanism during plastic flow in bcc alloys, dynamic strain ageing is seldom attributed to substitutional solutes [18,19,24,98,134], except perhaps at high temperatures and relatively high concentrations. In the case of interstitial solid solutions, solute diffusion is effectively athermal, in the sense that it is not the rate-limiting process and consequently kink-pair nucleation dictates the duration of the waiting time in between plastic events. Under such conditions, dislocation motion proceeds in a discontinuous manner, with rapid slip bursts punctuated by localized trapping of dislocation cores by solute clouds.

Clearly, in view of the processes involved, the study of the microscopic mechanisms of DSA requires atomic resolution. However, intrinsic bottlenecks of atomistic simulations

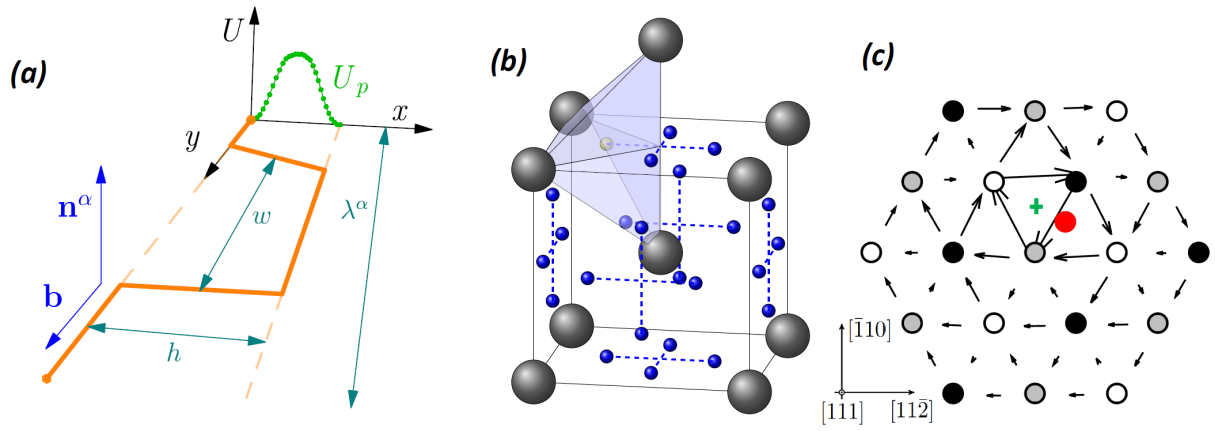

Figure 4.2: (a) Schematic diagram of the basic kink-pair geometry on the Peierls energy substrate $U_p(x)$. **b** and $\mathbf{n}^\alpha$ are the Burgers vector and the normal of the glide plane α. λ^α is the length of an arbitrary straight screw dislocation segment on the same plane, and h and w are the periodicity of the substrate potential and the stable kink-pair separation, respectively. (b) Elementary bcc lattice cell showing lattice atoms (in gray) and tetrahedral interstitial sites (in blue), including a shaded tetrahedron with the interstitial site highlighted in its center. (c) Differential displacement map obtained using DFT calculations [160] showing the stable configuration for the dislocation core-O complex (oxygen atom shown in red, core position shown in green). The resulting core structure changes from easy (no oxygen) to hard (with oxygen).

preclude their use for bridging the necessary time and length scale gap. In addition, the existence of kinks on screw dislocation segments in bcc crystals breaks the translational symmetry along the dislocation line, necessitating of full three-dimensional models to capture the wavelength of kink pairs along the line. This limits the applicability of techniques such as molecular dynamics (MD) to the mobility extremes of (i) stationary dislocations and highly mobile solutes (macroscopically equivalent to zero stress, high temperature conditions) and (ii) vice versa, mobile dislocations in a frozen solute field (high stress, low temperature). The case of bcc solid solutions poses extra challenges, as both governing mechanisms, i.e. solute diffusion and kink-pair nucleation, are considered rare events (albeit operating on different time scales). Discrete event simulations, on the other hand, offer the possibility of handling rare events over a broad time scale spectrum within a relatively simple framework [84, 117]. In this paper we show for the first-time dynamic simulations of dislocation-solute coevolution in tungsten crystals containing a few atomic parts per million (appm) of interstitial oxygen (W-O alloys). Here we use trace concentrations of oxygen in bcc W, specifically 0.2% (at.), consistent with nominally pure metals contaminated through exposure to the environment [11, 47]. Our simulations confirm that DSA occurs in a specific temperature-strain rate window that equalizes the timescales of solute transport and dislocation motion, resulting in intermittent slip and negative strain rate sensitivity. This kind of simulations has been made possible by the recent development of a kinetic Monte Carlo (kMC) model that accounts for thermally-activated kink-pair nucleation and solute diffusion via stress field coupling and short-range inelastic interactions [133, 162]. Our model is parameterized entirely using electronic structureatomic scale calculations, as described in previous works [160] (see Methods below) and is significantly more efficient than direct atomistic simulations. This allows us to study the relevant parameter space of stress, temperature, solute content, and dislocation line length to identify the conditions under which co-evolution occurs.

In bcc W, oxygen atoms diffuse with a migration energy of 0.2 eV on a tetrahedral sublattice (shown in Figure 4.2) [160]. This makes the W-O system peculiar among other interstitial bcc solid solutions, where generally octahedral diffusion is observed [57, 120]. When

dislocations are present, oxygen diffusion suffers a drift due to the underlying stress fields. In standard diffusion theory, this drift is characterized by an activation volume which when coupled to the stress yields the mechanical work to subtract from the activation energy for migration. In our case, the activation volumes of importance are approximately no larger than of an atomic volume, implying that O migration does not perturb the neighboring W atoms excessively. However, the trigonal distortions caused by oxygen atoms in their tetrahedral positions are neutralized near the screw dislocation core (see Figure 4.2), resulting in very stable bound structures with interaction energies of $1.5 \sim 1.8$ eV [79, 160]. Since this is on the order of the kink-pair activation enthalpy(≈ 1.6 eV), oxygen-dislocation dissociation events become the rate-limiting step when solute diffusion is sufficiently fast (and/or dislocation motion sufficiently slow) to allow for the formation of solute clouds (akin to the so-called *Cottrell* atmospheres) around dislocation segments. Depending on whether this is or not the case, three scenarios may be considered based on the nature of dislocation-solute interactions:

(i)A low stress and high temperature[1] regime where solute diffusion is favored over dislocation motion. One would then expect to see solute segregation at the dislocation core, i.e. solute atoms decorating the dislocation line with little or no dislocation glide. This is a widely studied scenario, both analytically and using atomistic methods [85,109,122,141,142], corresponding to an adiabatic process where dislocation motion occurs over timescales much longer than solute transport.

(ii)A high stress and low temperature regime where dislocation glide dominates over solute motion. In this case, the alloy behaves in the manner of a substitutional solid solution, with stationary solute atoms interacting with dislocation segments. This is expected to lead to conventional solute hardening, which has also been studied extensively in the literature by a number of different techniques [28, 30, 67, 81, 95, 111, 162].

(iii)An intermediate stress and temperature region where solutes and dislocations display

[1]Here, low and high, whether applied to stress or temperature, is meant relative to the shear modulus and melting point of the material in question.

similar mobilities and evolve on comparable timescales. It is in this region where DSA can occur [18,19]. However, such scenario has been comparatively much less studied using simulation methods (and even less so in bcc systems) owing to the intrinsic difficulties of treating two coevolving many-body systems. This can only be studied via numerical simulation [150] and is the primary subject of study in this work. In the following, we refer to this regime as the co-evolution regime.

It is worth noting that –in the above scenarios– stress equates strain rate by way of the relation $\sigma = C\dot{\epsilon}^m$. As mentioned above, the most reliable marker for the onset of serrated flow is in fact the observation of $m < 0$. The strain rate is obtained from the dislocation velocities calculated at each stress using Orowans equation, as

$$\dot{\epsilon}(\tau_{RSS}) = \rho_d b v(\tau_{RSS}) \tag{4.1}$$

where ρ_d is the dislocation density of the material, b is the modulus of the Burgers vector, and $v(\tau_{RSS})$ is the dislocation velocity, which depends on the resolved shear stress τ_{RSS} (see the Methods Section). In this fashion, when ρ_d is a realistic dislocation density (e.g. $\approx 1.4 \times 10^{14}$, as in ref. [131]), one can relate stress to strain rate by way of the stress dependence of the dislocation velocity. This value of d sets the dislocation line length to a magnitude of approximately $\lambda = (\rho_d)^{-1/2} = 400b$, which is used throughout the simulations.

Figure 4.3 shows all the applied stress-temperature conditions tested in our simulations as an applied stress-temperature map (τ_{RSS}–T) for an oxygen concentration of 0.2 %at. The different regions indicated on the map indicate the different flow behaviors observed as a result of the applied stress-temperature conditions. The yellow region containing τ_{RSS}–T points represented as black crosses delimits conditions where intermittent flow is observed (scenario (iii) above). Orange dots in the brown region mark simulations characterized by dislocations interacting with static solutes, while gray dots in the gray-shaded region are indicative of solute segregation at dislocation cores with little to no dislocation motion (scenarios (i) and (ii), respectively). The determination to ascribe a given τ_{RSS}–T point to a specific region was made by examining the combined behavior of the solute and the dislocation lines. The behavior of the solute is assessed by examining its mean square

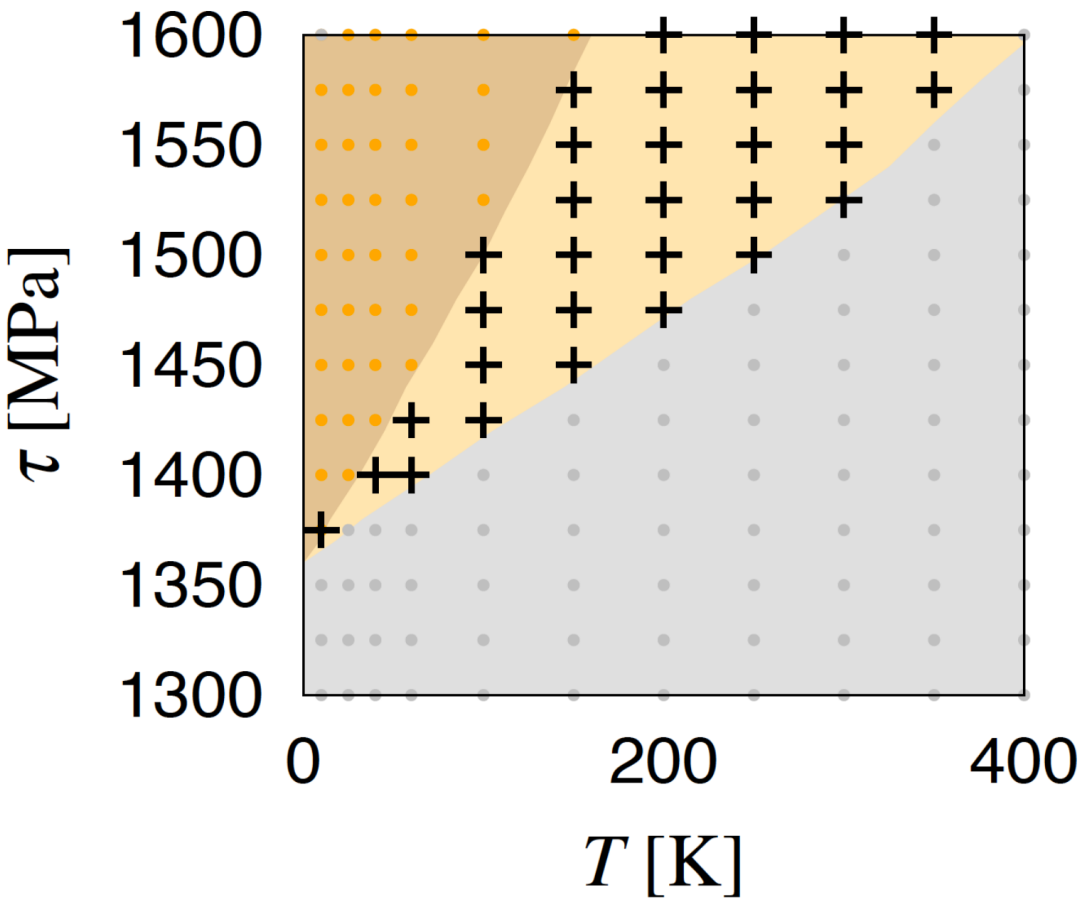

Figure 4.3: Stress-temperature map of all the simulation conditions considered. The yellow region containing -T points represented as black crosses delimits where intermittent flow is observed. Orange dots in the brown region mark simulations characterized by dislocations interacting with static solutes, while gray dots in the gray-shaded region are indicative of the formation of Cottrell atmospheres around dislocation cores with little to no dislocation motion.

displacement, $\langle \delta r^2 \rangle$ as a function of time, while that of the dislocation is evaluated by tracking the evolution of the kink-pair nucleation rate, r_{kp}, with time. Figure4.4: shows results for three characteristic stress-temperature points from Fig. 4, at 70, 250, and 600 K, all at 1.5 GPa of applied shear stress. The figure includes the expected kink-pair nucleation rate in a pure W crystal, represented for each τ_{RSS}–T point as a background shaded band in each graph. Spikes in r_{kp} are manifestations of local compositional and/or configurational variabilities along the dislocation line in time.

At a stress of 1.5 GPa and a temperature of 600 K (Fig. 4a), the dislocation at and the solute appear to move in an uncorrelated fashion, with the dislocation experiencing kink-pair nucleation rates similar to the reference pure state and the solute following a non-linear mean square displacement. At 1.5 GPa and 250 K (Fig. 4b), the solute is seen to undergo discontinuous motion, as revealed by a step-like mean square displacement, with the dislocation moving at a lower rate than in the homogeneous case and more kink-pair nucleation activity during stationary solute periods. At 1.5 GPa and 70 K (Fig. 4c), the solute becomes immobile and the dislocation moves through a static solid solution, with the kink-pair nucleation activity essentially following the homogeneous value with local spikes arising from dislocation-solute interactions.

While at 70 and 600 K, the average kink-pair nucleation rate r_{kp} agrees well with the background pure W value, at 250 K r_{kp} displays periods during which it is consistently lower than this background value. As well, the frequency of the local spikes is decreased with respect to the other two temperature cases. Correspondingly, the solute is seen to undergo an intermittent migration pattern, with periods of time where it is mostly stationary, and others characterized by rapid motion. Stress-temperature points displaying this general behavior are represented as black crosses in Fig. 3. We interpret this behavior as the precursor of dynamic strain ageing, where periods of reduced kink-pair nucleation activity are followed by stages of enhanced nucleation, leading to intermittent flow (whose macroscopic analog is *serrated flow* as in Fig. 1).

Figure 4.5 shows high-resolution images of the dislocation-solute system, showing only

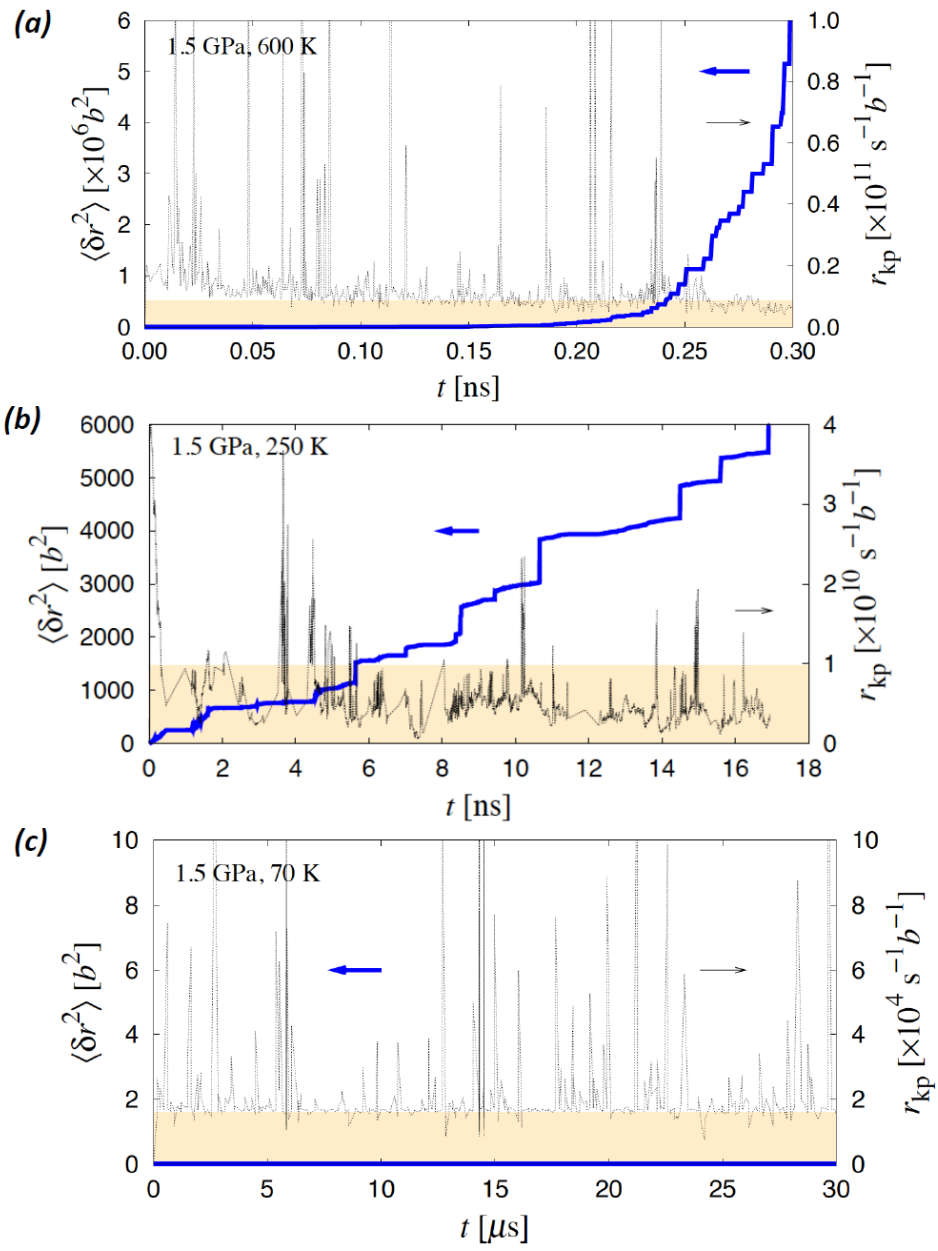

Figure 4.4: Evolution of the solute mean square displacement and kink-pair nucleation rates with time. The shaded band represents the equivalent kink-pair nucleation rate in pure W at each τ_{RSS}–T condition. (a) At a stress of 1.5 GPa and a temperature of 600 K. (b) At 1.5 GPa and 250 K. (c)At 1.5 GPa and 70 K.

dislocation segments and oxygen atoms. The images correspond to the three scenarios captured in Figs. 4a, 4b, and 4c. Kink-pairs can be appreciated along the dislocation line in all three cases. In the co-evolution regime (regime (iii)), the dislocation alternates episodes of solute pinning (as shown in Fig. 5b) with solute de-pinning, resulting in strain bursts marked by the formation of solute clouds around the dislocation core. Several kink-pairs in Fig. 5c coexist on two different glide planes due to the interaction between dislocation segments and static solutes, giving rise to the sporadic formation of cross-kinks [82]. A quantitative analysis of the solute density around the dislocation core for each of the three scenarios just described is also provided in the Supplementary Information 4.1.

It is common in the literature to express the flow behavior of dilute solid solutions displaying several deformation regimes as a strain rate-inverse temperature diagram highlighting the different regime transition boundaries. Figure 6a shows the $\dot{\epsilon}-(kT)^{-1}$ chart with the three different regimes just described as predicted by our simulations. The figure shows the DSA region colored in red, delimited by two dashed lines that bound the limits within which discontinuous slip takes place. The slope of these lines defines two activation energies [2], marked in the figure as 0.21 and 0.28 eV, that characterhaoize the operating mechanisms on each side of the DSA region. Given that the two principal processes governing the dislocation-solute system considered here are solute diffusion (with migration energies ranging between 0.15 and 0.20 eV) and kink-pair nucleation energies (ranging from 0 to 1.65 eV, see the Methods Section), the values shown in the graph can give an indication of the relative weight of each one on the overall dynamics. On the left side of the discontinuous flow region, the temperatures are sufficiently high to favor solute diffusion as the governing mechanism, with the value of 0.21 eV being consistent with this interpretation. On the right side, a higher energy of 0.28 eV suggests a more complex interplay between both processes, perhaps dominated by kink-pair nucleation next to oxygen atoms and more limited solute diffusivity.

Finally, as pointed out earlier, a principal signature of serrated flow is the existence of a negative strain rate sensitivity exponent (defining the correlation between the critical stress

[2]From the expression $\dot{\epsilon}\,(T) = \dot{\epsilon}_0 exp\left(-\frac{\Delta E}{kT}\right)$.

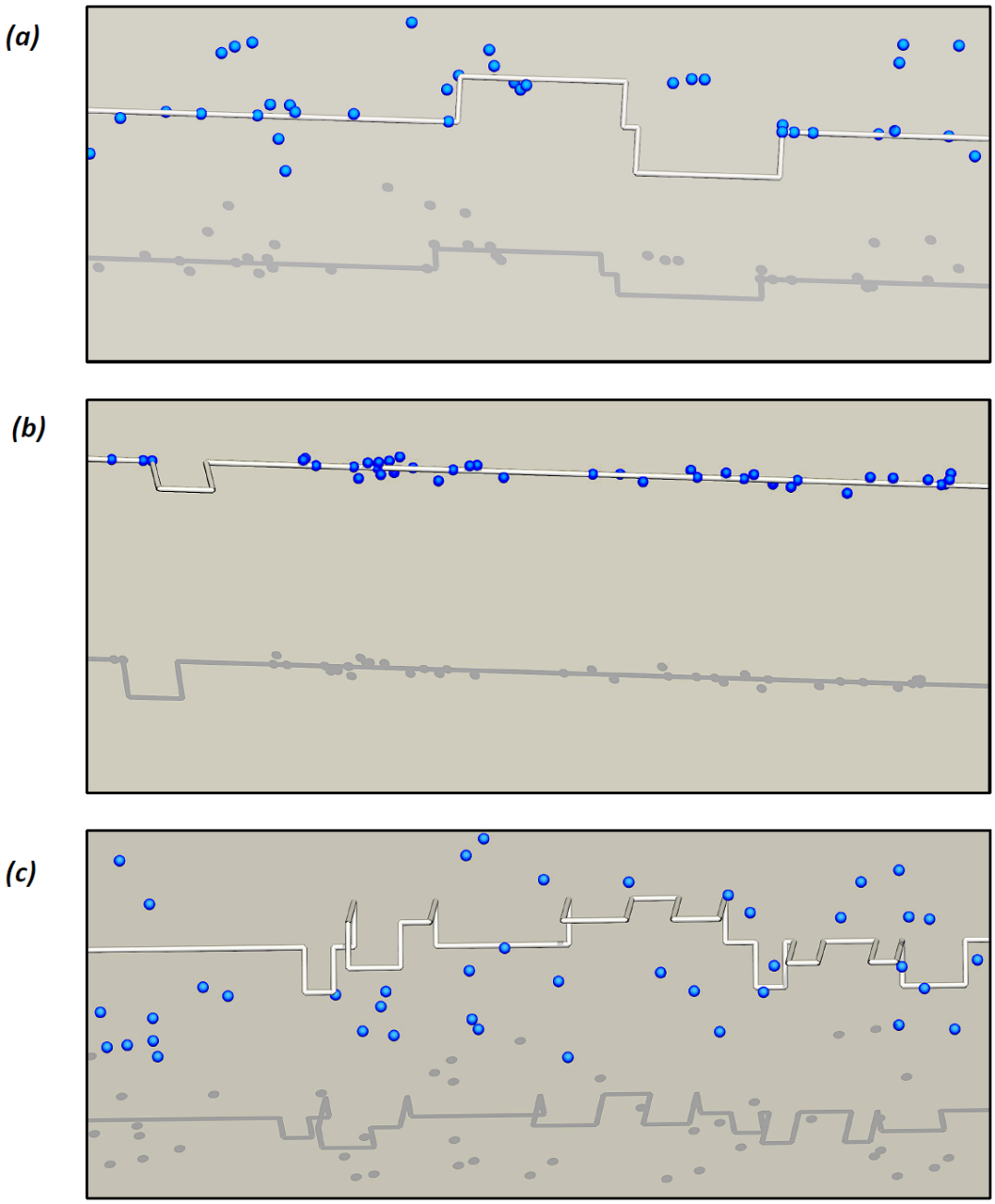

Figure 4.5: Simulation snapshots corresponding to the three scenarios shown in Fig. 4. Images (a), (b), and (c) match subfigures 4a, 4b, and 4c. (a) Solute diffusion occurs over time scales much shorter than kink-pair nucleation, making both processes effectively decoupled. (b) The oxygen atoms segregate at the dislocation core, temporarily trapping it before the dislocation can release itself and produce a strain burst. (c) No solute motion is observed, and the dislocation moves in a static interstitial solid solution, developing more kink-pairs and cross kinks.

and the strain rate). Our simulations are not performed under constant strain rate and thus m cannot be directly extracted from them. Instead, we fix the applied stress and measure the corresponding dislocation velocity. In this context, a negative m is equivalent to a stress-independent (or inversely proportional) dislocation velocity. Figure 4.6 shows stress-velocity curves for two temperatures that traverse the discontinuous flow regions shown in Fig. 3, 100 and 150 K. Even though the velocity axis is represented in logarithmic scale for ease of visualization, stress regions where the velocity is clearly independent or weakly dependent on stress can be appreciated. These stress intervals, which are marked with double arrows in the figure, are consistent with the DSA regions highlighted in Fig. 3. This is yet another piece of evidence strengthening the link between our simulation results and serrated plastic flow.

Given their focused scope, our simulations are not intended for representing bulk material behavior which is the context in which DSA is strictly defined, but they capture for the first time the interplay between mutually co-evolving dislocations and solute atoms in a way that allow us to explain observed macroscopic behavior. As such, they offer a unique window into the governing mechanisms behind serrated flow and the PLC effect. It must also be kept in mind that bcc metals display a set of particularities that call for the development of very specific approaches. One of these traits is the reduction of single crystal plasticity to the behavior of a single screw dislocation, as it has been amply demonstrated in a multitude of studies [16–19]. There are important implications of such result, as for example the observed equivalence between the DBTT activation energy and the kink-pair nucleation enthalpy in many bcc materials, which directly relates fracture behavior to screw dislocation properties [40, 41]. Thus, one can think of our model as descriptive of the characteristic behavior of dislocation sources in crystal grains of bcc materials, such that the total strain at the bulk level can be additively calculated from the different contributions of sources operating in the manner described here. This belongs to the of realm of (poly)*crystal plasticity* [70, 115], which is built as a crystal-level homogenization of fundamental physical mechanisms such as those revealed in this work. This serves to reinforce the notion that by understanding the

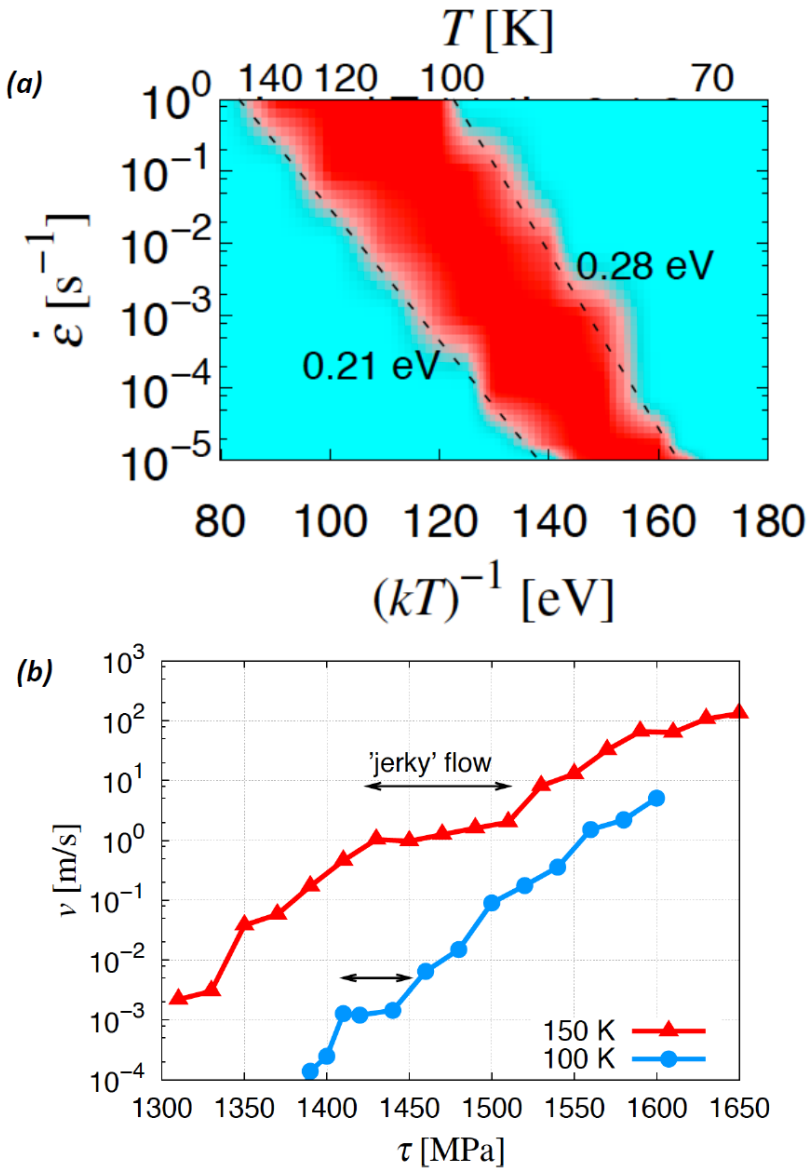

Figure 4.6: Color map of the strain rate-inverse temperature diagram obtained from our simulations.Each pixel in the figure is colored according to the propensity for jerky flow as defined in Fig. 4, with red and cyan indicating high and low propensities, respectively. The dashed lines correspond to two different fits of the general equations $\dot{\epsilon}\,(T) = \dot{\epsilon}_0 exp\left(-\frac{\Delta E}{kT}\right)$, with the values of ΔE given next to them.

physical mechanisms of screw dislocation-solute interactions, one can explain the observed macroscopic behavior.

In conclusion, we have shown using discrete stochastic models of dislocation-solute coevolution that jerky flow in dilute bcc interstitial solid solutions is a natural consequence of the dynamic interplay between the motion of solutes and dislocations. To capture such coevolution, the computational model must be capable of operating on diffusive time scales, i.e. above the characteristic atomic vibration period, on which thermally-activated processes take place. Our model is able for the first time to explore such regimes, exposing stress-temperature (or strain rate-inverse temperature) maps that define the dynamic behavior of the alloy. While these simulations pertain to one dislocation only, we are confident elevating the results reported here to the level of the microstructure, representing, e.g., the typical behavior of a source in bcc metals that issues dislocations with screw character one at a time. It is at that level then that dynamic strain ageing is defined, and where discontinuous flow can lead to localization and embrittlement.

4.1 Supplementary Information

This document contains additional analysis in support of our conclusions in the main manuscript Portevin-Le Chatelier effect observed through direct simulations of serrated flow in a body-centered cubic crystal. Here we provide a quantitative study the solute-dislocation behavior behind the three animation files supplied as supplementary information as well.

First, we track the solute density $\rho(r,t)$ as a function of distance to the dislocation core. To eliminate the time dependence and obtain a static picture of the solute distribution for ease of analysis, we discretize the space around the core into a series of concentric cylindrical volumes increasing in thickness by an amount b. This is schematically depicted in Figure S1. We then time average the solute concentration within each cylindrical slice as:

$$c\,(r) = \frac{1}{t'}\int_0^{t'} \rho(r,t)dt$$

So that $c\,(r)$ is a 'still' picture of the solute radial distribution around the dislocation

core averaged over a sufficiently long-time t'. It must be noted, however, that the position of the dislocation itself changes with time, and so r is referred to a local frame of reference with origin at the dislocation center of mass $\mathbf{COM}(t\ )$:

$$r = r^{'} - COM(t)$$

where $r^{'}$ is the location of a solute atoms referred to a global coordinate system, and bold script indicates vectorial quantities in three dimensions. Note that the function(s) $\mathbf{COM}(t\ )$ are a direct output of the kinetic Monte Carlo simulations. The above two equations are linked by $r = \|\mathbf{r}\|$. This analysis is done in a highly dynamic environment, with solute atoms moving in and out of each cylindrical slice either by direct diffusion or as the dislocation moves in space and r changes. Then, we count how many solute atoms occupy each slice at each time and then divide by the slice volume to obtain the solute density:

$$\rho\,(r,t) = \frac{n(r,t)}{V(r)}$$

However, for the discretization mentioned above, this density can be simplified as:

$$\rho\,(m,t) = \frac{n(m,t)}{\pi b^2 L(2m+1)}$$

Where L is the total dislocation length (equal to $400b$ in this work) and m is the slice index of thickness $b(m\ =1,\ldots 6$, see Fig. 4.7). We then apply this analysis in a series of simulations at the same temperature of 150 K varying the stress to encompass the three regions of dynamic behavior depicted in Figure 4.3 of the main manuscript.

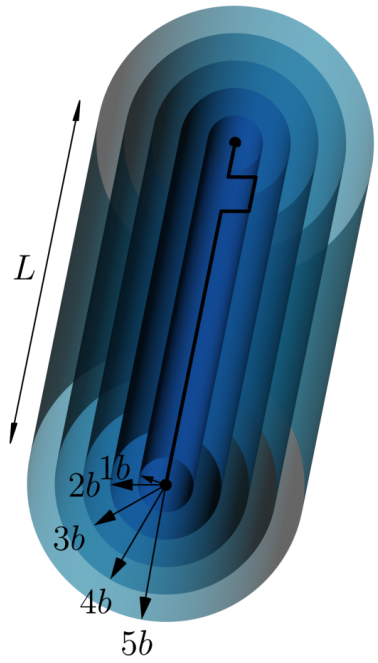

Figure 4.7: Schematic diagram showing the discretization of volume around the dislocation line into cylindrical slices to track the dynamic evolution of solute. The dislocation line length is L, and a kink-pair is shown for descriptive purposes.

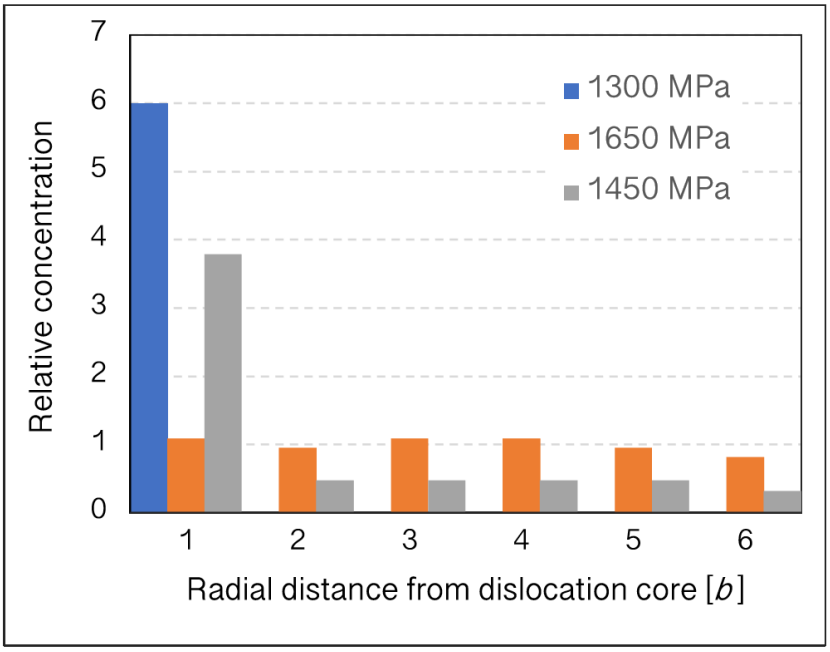

Figure 4.8: Solute concentration histogram showing the average distribution of oxygen atoms around the dislocation core expressed relative to the alloy composition of 0.2% at. The data correspond to three different simulations at 1300, 1450, and 1650 MPa, all at 150 K. These distributions are time-averaged over several ns of simulation. As such, the data represent spatially and time integrated results.

CHAPTER 5

Implementation Details of Kinetic Monte Carlo Simulations

5.1 Elastic energy of a piecewise kinked dislocation

5.1.1 Self-energy of a straight dislocation segment

The non-singular expression for the self-energy of a straight dislocation segment $\mathbf{m}$ defined by endpoints x_1 and x_2, and Burgers vector b is:

$$W_{self}(\mathbf{m}) = \frac{\mu}{4\pi(1-\nu)} \left\{ (b^2 - \nu(\mathbf{b}\cdot\mathbf{t})^2) L ln \left[\frac{L_a + L}{a} \right] - \frac{3-\nu}{2} (\mathbf{b}\cdot\mathbf{t})^2 (L_a - a) \right\} \qquad (5.1)$$

where

$$L = \|\mathbf{x}_2 - \mathbf{x}_2\|$$

$$\mathbf{t} = \frac{\mathbf{x}_2 - \mathbf{x}_2}{L}$$

and

$$L_a = \sqrt{L^2 + a^2}$$

and a is the so-called *corewidth* over which the Burgers vector spreads.

Sometimes, when$L$ is of the order of a, as for kink segments, the self-energy is better computed via atomistic methods.

5.1.2 Interaction energy between two dislocation segments

The general expression for the interaction energy of two segment **m** and **n** with, respectively, endpoints$\mathbf{x}_1$ and $\mathbf{x}_2$, and $\mathbf{x}_3$ and $\mathbf{x}_4$ is:

$$W_{int}(\mathbf{m},\mathbf{n}) = W^*(\mathbf{x}_4-\mathbf{x}_2) + W^*(\mathbf{x}_3-\mathbf{x}_1) - W^*(\mathbf{x}_4-\mathbf{x}_1) - W^*(\mathbf{x}_3-\mathbf{x}_2) \tag{5.2}$$

where the functional W^* takes different forms depending on the nature of the interaction. In the following, expressions for parallel and non-parallel segments are provided. In both cases, the common Burgers vector to both segments is **b**.

5.1.3 Non-parallel segments

This is relevant for the interaction between kink segments and screw segments. The energy functional $W^* \equiv W_{np}(\mathbf{x})$ is defined as:

$$\begin{aligned} W_{np}(\mathbf{x}) = \frac{\mu}{4\pi(1-\mu)(\mathbf{u}\cdot\mathbf{u})}(&\mathbf{x}\cdot ln\left[R_a + \mathbf{x}\cdot\mathbf{t}^{'}\right]((\mathbf{A}_1-\mathbf{A}_2^{'})v^{'} + A_3^{'}\mathbf{u}) + \\ &\mathbf{x}\cdot ln\left[R_a+\mathbf{x}\cdot\mathbf{t}\right](\mathbf{A}_1-\mathbf{A}_2)\mathbf{v} + \mathbf{A}_3\mathbf{u}) + \mathbf{A}_4R_a + \\ &\frac{(A_1-A_5)(2(\mathbf{x}\cdot\mathbf{u})^2+(\mathbf{u}\cdot\mathbf{u})a^2)}{\sqrt{(\mathbf{x}\cdot\mathbf{u})^2+(\mathbf{u}\cdot\mathbf{u})a^2}} arctan(\frac{(1+\mathbf{t}\cdot\mathbf{t}^{'})R_a + \mathbf{x}(\mathbf{t}+\mathbf{t}^{'})}{\sqrt{(\mathbf{x}\cdot\mathbf{u})^2+(\mathbf{u}\cdot\mathbf{u})a^2}})) \end{aligned} \tag{5.3}$$

where $t = (\mathbf{x}_2-\mathbf{x}_1)/L_m$ and $t^{'} = (\mathbf{x}_4-\mathbf{x}_3)/L_n$ are the respective line tangents(L_m =

$\|\mathbf{x}_2 - \mathbf{x}_1\| and L_n = \|\mathbf{x}_4 - \mathbf{x}_3\|)$, $\mathbf{u} = \mathbf{t} \times \mathbf{t}\prime, \mathbf{v}' = \mathbf{t}' \times \mathbf{u}$, and:

$$
\begin{aligned}
R_a &= \sqrt{\mathbf{x} \cdot \mathbf{x} + a^2} \\
A_1 &= (1+\nu)(\mathbf{b} \cdot \mathbf{t})(\mathbf{b}' \cdot \mathbf{t}') \\
A_2 &= (b^2 + (\mathbf{b} \cdot \mathbf{t})^2)(\mathbf{t} \cdot \mathbf{t}') \\
A_2' &= (b^2 + (\mathbf{b} \cdot \mathbf{t}')^2)(\mathbf{t} \cdot \mathbf{t}') \\
A_3 &= 2(\mathbf{b} \cdot \mathbf{u})(\mathbf{b} \cdot \mathbf{v}) \frac{\mathbf{t} \cdot \mathbf{t}'}{\mathbf{u} \cdot \mathbf{u}} \\
A_3' &= 2(\mathbf{b} \cdot \mathbf{u})(\mathbf{b} \cdot \mathbf{v}') \frac{\mathbf{t} \cdot \mathbf{t}'}{\mathbf{u} \cdot \mathbf{u}} \\
A_4 &= ((\mathbf{b} \cdot \mathbf{t})(\mathbf{b} \cdot \mathbf{v}) + (\mathbf{b} \cdot \mathbf{t}')(\mathbf{b} \cdot \mathbf{v}'))(\mathbf{t} \cdot \mathbf{t}') \\
A_5 &= 2(\mathbf{b} \times \mathbf{u})^2 \frac{\mathbf{t} \cdot \mathbf{t}'}{\mathbf{u} \cdot \mathbf{u}}
\end{aligned}
\tag{5.4}
$$

where $b = \|\mathbf{b}\|$. These expressions simplify significantly for perpendicular segments.

5.1.4 Interaction energy between two parallel segments

This interaction includes the interaction of segments of pure screw character with one another and the interaction of kink segments of the same kind with one another. As above, the Burgers vector is assumed to be the same for all segments. The interaction energy functional has the form$W^*(\mathbf{x}) \equiv W_{\|}(\mathbf{x})$:

$$
\begin{aligned}
W(\mathbf{x}) = &\frac{\mu}{4\pi(1-\nu))}((2b(\mathbf{b} \cdot \mathbf{x}) - b^2(\mathbf{t} \cdot \mathbf{x})(3-\mu))ln(R_a + \mathbf{t} \cdot \mathbf{x}) + R_a b^2(2-\nu) - \\
&\frac{R_a}{2} \frac{(\mathbf{b} \cdot \ \mathbf{x} - b\mathbf{t} \cdot \mathbf{x})^2 - a^2 b^2(\nu - 1)}{R_a^2 - (\mathbf{t} \cdot \mathbf{x})^2})
\end{aligned}
\tag{5.5}
$$

where /bf t is the common line tangent to both segments. From Sections 1.1 and 1.2, the total elastic energy for a dislocation discretized into N segments is then:

$$
E = \sum_i^N (W_{self}^i + \sum_{j>i}^N W_{int}^{ij}) \tag{5.6}
$$

The problem of computing the total elastic energy is then $O(\frac{N^2}{2})$. Later, it will be discussed how to reduce it to $O(N)$. When using periodic boundary conditions,eq. 5.6 must include

periodic image contributions. This will also be dealt with later.

5.2 Stress tensor from a dislocation segment

In the non-singular elastic formulation, the stress tensor at a point $\mathbf{x}$ from a straight dislocation segment defined by endpoints $\mathbf{x}_1$ and $\mathbf{x}_2$ and Burgers vector $\mathbf{b}$ is:

$$\sigma_d(\mathbf{x}) = \mathbf{T}(\mathbf{x} - \mathbf{x}_1) - \mathbf{T}(\mathbf{x} - \mathbf{x}_2) \tag{5.7}$$

where the function T is defined as:

$$\begin{aligned}\mathbf{T}(\mathbf{x}) =& \frac{\mu}{4\pi(1-\nu)}(((\mathbf{x}\times\mathbf{b})\cdot\mathbf{t})(A_1(\mathbf{x}\otimes\mathbf{x}+\mathbf{x}\otimes\mathbf{t})+A_3(\mathbf{t}\otimes\mathbf{t})+A_4\mathbf{I})+\\ & A_5((\mathbf{x}\times\mathbf{b})\otimes\mathbf{t}+\mathbf{t}\otimes(\mathbf{x}\times\mathbf{b}))+A_6((\mathbf{t}\times\mathbf{b})\otimes\mathbf{x}+\mathbf{x}\otimes(\mathbf{t}\times\mathbf{b}))\\ & +A_7(\mathbf{t}\times\mathbf{b})\otimes\mathbf{t}+\mathbf{t}\otimes(\mathbf{t}\times\mathbf{b}))\end{aligned} \tag{5.8}$$

where

$$\mathbf{t} = \frac{\mathbf{x}_2 - \mathbf{x}_1}{\|\mathbf{x}_2 - \mathbf{x}_1\|}$$

$$A_1 = -\frac{\mathbf{x}\cdot\mathbf{t}(3R_a^2 - (\mathbf{x}\cdot\mathbf{t})^2)}{(R_a^2 - (\mathbf{x}\cdot\mathbf{t})^2)^2 R_a^3}$$

$$A_2 = R_a^{-3} - (\mathbf{x}\cdot\mathbf{t})A_1$$

$$A_6 = -\frac{(\mathbf{x}\cdot\mathbf{t})A_1}{R_a(R_a^2 - ((\mathbf{x}\cdot\mathbf{t})A_1)^2)}$$

$$A_3 = -R_a^{-3}\mathbf{x}\cdot\mathbf{t} + A_6 + (\mathbf{x}\cdot\mathbf{t})^2 A_1$$

$$A_4 = A_6 + a^2 A1$$

$$A_5 = (\nu-1)(A_6 + \frac{a^2}{2}A_1)A_7 = \frac{\nu}{R_a} - (\mathbf{x}\cdot\mathbf{t})A_6 - \frac{a^2(1-\nu)}{2}A2$$

and I is the identity tensor.

As for the energies,the total stress tensor at a point $\mathbf{x}$ from a dislocation discretized into N segments is then:

$$\sigma(\mathbf{x}) = \sum_i^N \sigma_i(\mathbf{x}) \tag{5.9}$$

Computing the total self stress along the dislocation is then $O(\frac{N^2}{2})$ as well. Computing it at a specific location(solute atom, one dislocation segment) is $O(N)$. When using periodic boundary conditions, this equation must also include periodic image contributions, as for the energy.

5.3 Free energy of a double kink

The nucleation rate of a kink pair can be defined as:

$$j_{kp} = \nu_0 \exp(-\frac{\Delta F_{kp}}{2kT}) \tag{5.10}$$

where ν_0 is an attempt frequency, and ΔF_{kp} is the (Gibbs) free energy difference resulting from the nucleation of an *embryonic* kink pair, i.e. one with the minimum lattice separation. The $\frac{1}{2}$ factor arises from the fact that it is only necessary to take the dislocation to the activated state (saddle point) to achieve a transition. As we shall see, this is only appropriate for cases where the free energy landscape is symmetric about the midpoint of the reaction coordinate. In the more general case, this landscape is not symmetric and the energies must be computed up to the relevant limits. In this section we calculate all the contributions to δF_{kp} without assuming symmetric free energy landscapes. The free energy can be defined as:

$$\Delta \mathbf{F}_{kp} = \Delta \mathbf{H} - \mathbf{T}\Delta \mathbf{S} = \sum_i \Delta \mathbf{E} i - \Delta \mathbf{W}_m - \mathbf{T}\Delta \mathbf{S} \tag{5.11}$$

where $\Delta \mathbf{H}$ is the enthalpy,$\Delta \mathbf{E}_i$ are the different contributions to the internal energy difference, W_m is the work done by the applied stress, T the temperature and $\Delta \mathbf{S}$ the entropy. Let us address each of these one by one in the following sections.

5.3.1 Contributions to the internal energy

Here we consider only two contributions to the internal energy, namely, the elastic energy and the *substrate* energy. There is a third contribution -the core energy-that is not symmetric with respect to the kink sense, but we ignore this contribution here. The elastic energy of a

double kink as the energy difference between the dislocation in the state prior to a kink pair being nucleated$\mathbf{E}(\mathbf{i})$, and that containing the new kink pair $\mathbf{E}(\mathbf{j})$:

$$\Delta\mathbf{E}_{el} = \mathbf{E}(\mathbf{j}) - \mathbf{E}(\mathbf{i}) \tag{5.12}$$

where $\mathbf{E}(\mathbf{i})$and $\mathbf{E}(\mathbf{j})$ are computed using eq.5.6. For its part, the substrate energy reflects the lattice resistance to the nucleation of akink pair in the form of a periodic energy landscape $\mathbf{V}_p(x)$ (for simplicity, in his section we assume that$x$ and y are the coordinates perpendicular and parallel to the screw direction on the plane $\mathbf{n}$ of the kink pair). The dislocation must overcome this landscape in order to get over to the next periodic energy minimum. The substrate energy is defined as:

$$\Delta\mathbf{E}_s = \int_i^j V_p(x)dl \tag{5.13}$$

where dl is the differential line element that runs from state $\mathbf{i}$ to state $\mathbf{j}$. This integral can be broken into two kink segements and one staight segment separating them. If we define $V_p(x)$ as a sinusoidal function

$$V_p(x) = E_p sin\frac{\pi x}{h} \tag{5.14}$$

where E_p is the amplitude, also known as $Peierls$ energy, and h is the kink $height$, then one can write ΔE_s as:

$$\Delta E_s = E_p\omega + 2\int_0^h E_p sin\frac{\pi x}{h}dl = E_p(\omega + \int_0^h sin\frac{\pi x}{h}dl) \tag{5.15}$$

where ω is the kink pair separation($\omega \equiv d$, the lattice distance distance along the screw direction, for embryonic kinks),h is the so-called kink height, and $dl = \sqrt{dx^2 + dy^2}$. The factor of 2 reflects the fact that there are two kinks in a kink pair. To solve this integral, one need specify the line equation for a kink segment and use it to eliminate one of the variables x or y. Alternatively, one can compute this energy using atomistic methods. For example, the energy for a kink pair separated an infinite distance has been calculated to be 1.70 eV(including elastic interactions that should be accounted for) for the MEAM potential for W. When V_p is also a function of stress, a simple sinusoidal function may not be sufficient to describe it. In such cases, the value of E_p is the maximum amplitude of the $V_p(x, \boldsymbol{\sigma})$function

over the entire integration range(reaction coordinate), which needs to be obtained by way of atomistic methods. For subsequent sections, the point at which$V_p(x, \boldsymbol{\sigma})$ function over the entire integration range(reaction coordinate), which needs to be obtained by way of atomistic methods. For subsequent sections, the point at which $V_p(x, \boldsymbol{\sigma})$ is maximum, let us call it $E_p^{'}$, will be denoted by x_p. Then, more generally, under a situation of applied stress:

$$\Delta E_s = E_p^{'} d + 2 \int_0^{x_p} V_p(x, \boldsymbol{\sigma}) dl \tag{5.16}$$

where it is noted that the integration limit has changed to the point of activation. This effect has been calculated directly by atomistic calculations for W-MEAM and has been found to be quite small.

Perhaps a more efficient way to take care of the entire $\Delta \mathbf{H}$ term is to use the following expression:

$$\Delta H = \Delta H_0 (1 - signof(\sigma_{RSS}) \sqrt{\frac{|\sigma_{RSS}|}{\tau_p}})^{1.25} \tag{5.17}$$

where:

$$\Delta H_0 = 1.70eV$$
$$\tau_p = 3.2GPa \tag{5.18}$$

and σ_{RSS} will be defined in next section. Equation 10 is from a model that captures the correct asymptotic behavior as$\sigma_{RSS} \to 0$ and $\sigma_{RSS} \to \tau P$. One can use atomistic calculations in the intermediate stress regime to adjust eq. 5.17 to include all energy contributions while respecting the correct asymptotics.

5.3.2 Mechanical work

The mechanical work $\Delta\ W_m$ is obtained by calculating the work done by the Peach-Kohler force, f_{PK}, in taking the dislocation from state i to j:

$$\Delta W_m(\mathbf{i} \to \mathbf{j}) = f_{PK} \Delta A(\mathbf{i} \to \mathbf{j})$$

The force per unit length can be calculated by contracting the stress and Schmid tensors:

$$f_{PK} = \boldsymbol{\sigma} : \mathbf{S}$$

where

$$\mathbf{S} = \frac{(\mathbf{b} \otimes \mathbf{n}) + (\mathbf{n} \otimes \mathbf{b})}{2}$$

The area $\Delta A(\mathbf{i} \to \mathbf{j})$ is simply the extra area created by taking the embryonic kink to the activated state, i.e. $\Delta A = x_p d$. Alternatuvely, this force can be obtained by calculating the resolved shear stress(RSS) on the slip system defined by slip direction $\mathbf{t}$ and normal $\mathbf{n}$. In this case, both $\mathbf{t}$ and $\mathbf{n}$ are unit vectors(the slip direction is simply $\mathbf{t} = \mathbf{b}/b$, where $b = \|\mathbf{b}\|$):

$$\sigma_{RSS} = \mathbf{t} \cdot \boldsymbol{\sigma} \cdot \mathbf{n} \tag{5.19}$$

And then:

$$f_{PK} = b\sigma_{RSS}$$

The stress tensor σ at a given point $\mathbf{x}$ is defined as:

$$\boldsymbol{\sigma} = \boldsymbol{\sigma}_{app}(\mathbf{x}) + \boldsymbol{\sigma}_d(\mathbf{x}) \tag{5.20}$$

i.e. it contains contributions from the applied stress, typically assumed to be uniform(not dependent on $\mathbf{x}$), and the dislocation stress.

5.3.3 Entropy

The entropy is unknown but sometimes taken as $\Delta S = 3k$, where k is Boltzmann's constant.

5.4 Sustainable kink pair nucleation of width n

This section explains how to obtain nucleation rates of kink pairs of prescribed separation. For an existing kink pair of width ω, the change in energy associated with going from state ω to state$(\omega + 1)$(i.e. to widen by one lattice spacing)is $\Delta F_{kp} = F_{kp}(\omega + 1) - F_{kp}(\omega)$. Then,

the rate for kink pair to increase its separation by one lattice spacing, i.e. changing state $\omega \to \omega + 1$ is:

$$r_+(\omega) = \nu_0 exp(-\frac{(F_{kp}(\omega+1) - F_{kp}(\omega))/2 + U_m}{kT})(1 + H(\omega)) \tag{5.21}$$

whereU_m is the energy barrier for kink migration, which is typically quite low. Identically, the rate for a kink pair to reduce its separation by one lattice spacing or $\omega \to \omega - 1$ is:

$$r_+(\omega) = \nu_0 exp(-\frac{(F_{kp}(\omega-1) - F_{kp}(\omega))/2 + U_m}{kT})(1 + H(\omega-1)) \tag{5.22}$$

$H(\omega)$ is a step function:

$$\begin{cases} 0 & \omega \leq 0 \\ 1 & 1 \leq \omega \end{cases}$$

that accounts for the fact that when the kink pair is separated by a distance larger than 1, both kinks can contribute to growth or shrinkage, and, also, than when the kink pair is embryonic, only one of the kinks can move to shrink it. The total rate to escape state ω is

$$r_0(\omega) = r_+(\omega) + r_+(\omega)$$

while the probability to undergo the$\omega \to \omega + 1$ transition is:

$$F(\omega) = \frac{r_+(\omega)}{r_0(\omega)}$$

The rate to nucleate embryonic kinks is then the rate to go from state $0 \to 1$,i.e

$$J(1) \equiv r_+(0) = \nu_0 exp(-\frac{F_{kp}(1)}{2kT})$$

where the full calculation of F_{kp} is given in Section 5.3. The $\frac{1}{2}$ factor again assumes that the energy landscape is a symmetric function. A more realistic description, which will be used here, is given in Section 5.3.

Working with embryonic kinks only is very inefficient, because when they are so close together most of them just annihilate again and the system is unchanged. The idea here is to compute the rate $J(n)$ at which double kinks of separation n¿1 are nucleated so that the time that is takes for a kink pair of size $\omega = 1$ to expand to a size of $\omega = n$ is already factored

into the nucleation rate and CPU time does not have to be wasted sampling self-annihilation events.

$J(n)$ can be written as the rate at which embryonic kinks survive to expand to width n,i.e.:

$$J(n) = J(1)p_s(1 \to n)$$

where $p_s(i \to j)$ is the probability for a kink pair with ω to expand to$\omega = j$ before annihilating. In this context, $i \geq 1$. p_s can be written as the product of the probability to go from state $\omega = 1$ to state $\omega = 2$, times the probability to go from state$\omega = 2$ to state $\omega = 3$, and so on, times the probability to go from state $\omega = n - 1$ to state $\omega = n$, i.e.:

$$p_s(1 \to n) = \prod_{k=1}^{n} p_s(k \to k+1) \tag{5.23}$$

To go from k to $k + 1$, two things can happen:either a kink goes from k to $k + 1$ directly with probability $F(k)$, or the kink pair first shrinks to $k-1$ with probability $1-F(k)$. From k-1 the kink again can either go to k and start from there, or further shrink to k-2 with probability 1-F(k-1) and start from there, and son and so forth. This recursive process can be written as:

$$\begin{aligned}
&p_s(k \to k+1) = F(k)+ \\
&((1 - F(k))p_s(k-1 \to k)p_s(k \to k+1)+ \\
&(1 - F(k-1))p_s(k-2 \to k-1)p_s(k-1 \to k)p_s(k \to k+1)+ \\
&\dots) \\
&= F(k) + p_s(k \to k+1)(\sum_{i=1}^{k}(1 - F(i)) \prod_{j=i-1}^{k-1} p_s(j \to j+1))
\end{aligned} \tag{5.24}$$

Therefore:

$$p_s(k \to k+1) = \frac{f(k)}{1 - (\sum_{i=1}^{k}((1 - F(i)) \prod_{j=i-1}^{k-1} p_s(j \to j+1))} \tag{5.25}$$

If one discards second-order jumps,i.e. those that take the kink back beyond state$k - 1$, we arrive at the more compact expression:

$$p_s(k \to k+1) = \frac{F(k)}{1 - (1 - F(k))p_s(k-1 \to k)} \tag{5.26}$$

Using the initial condition $p_s(0 \rightarrow 1) = 0$ all the surviving probabilities can be computed recursively using eqs.5.25 or 5.26, and plugged into eq.5.23 to obtain $J(n)$.

This section gives closed-form expressions to calculate the nucleation rate of kink pairs separated by a distance nd. Because the survival probabilities can be quite low,$J(n)$ will be significantly smaller than J(1),but the efficiency of the simulations will increase notably. From what I have seen, the simulations do not show a strong dependence on the choice of n, although it should not be overly large compared to the total dislocation length.

5.5 Efficient elastic energy updates

There are two situations where the elastic energy of the dislocation must be computed. The first instance is when the nucleation rates of embryonic kinks on every available segment need to be calculated. The second one is when an event (either kink pair nucleation or kink propagation) is executed and the elastic energy of the resulting dislocation needs to be updated. We treat those two separately below.

5.5.1 Efficient calculation of nuleation rates

As shown above, the cost to compute the elastic energy of a given state of teh dislocation line scales as $O(N^2)$. Computing the nucleation rate for each segment along the line during each Monte Carlo step requires that energy of N different states be calculated, which results in an $O(N^3)$ process$N$ states times the cost of calculating the energy of each state, which is N^2). This obviously is prohibitive computationally. However, it turns out that, from a given reference state whose elastic energy is known, the changes in elastic energy due to an embryonic kink pair nucleated on a given segment is simply equal to the interaction energy of that unit loop with all the other N segments in the line. The interaction energy of the loop consists of calculating the interaction energies of each of the four loop sides with each of the N segments of the dislocation line. This corresponds to $NO(1)$ processes. Because this has to be done for each available nucleation site, of which there are N, the total cost of

this calculation is $O(N^2)$. This reduces the order of magnitude of the computational cost by one.

5.5.2 Elastic energy updates of the reference state

Once an event is selected and executed, updating the total elastic energy of the dislocation is simply a matter of summing the self-energy of the corresponding embryonic loop plus the work required to insert that loop in the stress field of the parent dislocation:

$$\Delta E_{el} = E_{loop}^{self} + W_{loop}^{\sigma} \tag{5.27}$$

The calculation of E_{loop}^{self} is a $O(1)$ process because the self-energy of the loop involves the calculation of four segment self-energies plus six interaction energies(cf.Section 1). For this calculation, the line sense of the loop must coincide with that of the orginal dislocation.

For its part,the mechanical work to insert the loop can be calculated assuming a cartesian reference system with z along the screw direction, y parallel to the glide plane normal, and x parallel to the reaction direction. For an infinite straight screw dislocation along the z axis with $b \equiv (0, 0, b)$ the non-singular solution for the stress field is:

$$\sigma_{xz} = -\frac{\mu b}{2\pi}\frac{y}{R_a^2}(1 - \frac{a^2}{R_a^2}) \tag{5.28}$$

and

$$\sigma_{yz} = -\frac{\mu b}{2\pi}\frac{x}{R_a^2}(1 - \frac{a^2}{R_a^2}) \tag{5.29}$$

where $R_a = \sqrt{x^2 + y^2 + a^2}$ and a is the core width. The work done to create a loop in the stress field of its parent screw dislocation can be calculated from the following integral:

$$W_{loop}^{\sigma} = b \int \sigma_s(x, y) dA \tag{5.30}$$

where dA is the surface area differential on the glide plane for a kink pair of separation nd,i.e.:

$$dA = (nd)dx$$

and the integral can be reduced to the stress component with a x dependence only:

$$W^{\sigma}_{loop} = bd \int \sigma_{yz} dx = -\frac{\mu b^2 nd}{2\pi} \int \frac{x}{R_a^2}(1 - \frac{a^2}{R_a^2})dx \tag{5.31}$$

whose analytical solution is:

$$W^{\sigma}_{loop} = -\frac{\mu b^2 nd}{4\pi}(\frac{a^2}{a^2 + x^2} + ln(a^2 + x^2)) \tag{5.32}$$

Integrated over the $(0, h)$ interval, this results in:

$$W^{\sigma}_{loop} = \frac{\mu b^2 nd}{4\pi}(\frac{a^2}{a^2 + h^2} - ln(1 + \frac{h^2}{a^2})) \tag{5.33}$$

which reduces to $W^{\sigma}_{loop} \approx \frac{\mu b^2 nd}{4\pi}(\frac{1}{2} + ln2) = 1.19\frac{\mu b^2 nd}{4\pi}$ when $h \approx a$.

Computing the nucleation rate in one of the N dislocation segments from the last dislocation state reduces to calculating the last executed event. Again, this is an$O(1)$ process repeated N times so that the entire calculation of the nucleation rates becomes $O(N)$.

5.6 Using periodic boundary conditions

The use of periodic boundary conditions(PBC) affects only the calculation of the elastic energies. In principle, one must compute the interaction energy of any guven segment with all the segments of the infinite array of periodic images that result from the use of PBC. The range of dislocation-dislocation interactions varies as r^{-1} and therefore no possibility of truncation exists, which makes the infinite sums divergent. In that case, because the range of loop interactions decays as r^{-3}, it is shown that it is sufficient to adopt the *minimumimageconvention*(MIC) to have convergent sums. The MIC allows us to have each segment interact only once with the segments of the adjacent images:

$$d^{'}_{ij} = |\mathbf{x}^{'}_{j} - \mathbf{x}_i|$$

where the ' refers to an *image* segment and $\mathbf{x}^{'}_{j}$ is either equal to $\mathbf{x}_j \pm L$. The MIC states that: if $d^{'}_{ij} > \frac{L}{2}$, then $d^{'}_{ij} = \frac{L}{2} - d^{'}_{ij}$

In other words, segment i of the physical dislocation line interacts only once with segment j of the image dislocation lines, that which is closest to it. Assuming we compute this extra *image* elastic energy for each segment i then eq.5.6 becomes:

$$E = \sum_{i}^{N}(W^{i}_{self} + \sum_{j>i}^{N}(W^{ij}_{int} + W^{ij^{'}}_{int})) \tag{5.34}$$

where $ij^{'}$ refers to the pair formed by segment i and image segment$j$.

5.7 Treatment of solute interactions

5.7.1 short range interaction

When the solute is within the reaction distance of a dislocation segment, then we cannot use the elastic(or 'long' distance) treatment used in the above subsections. Instead, we must assume that core effects are dominant and treat the dislocation and the solute as bound with a binding energy E_b(which, again, may be negative). This energy simply adds to ΔF_{kp} in eq.5.10,i.e. an extra energy E_b is required for the dislocation to overcome the solute atom. In the case when a kink encounters the solute atom, the kink motion must now be treated as diffusive. That means that E_b must be added to U_m in eq.5.21 if kink motion was already being considered diffusive, or the ballistic motion of a kink must be arrested whenever it encounters a solute in its path, and treated diffusively at that point. Once the kink is released from the solute, it can be treated ballistically agian. The binding energy E_b must again be computed using electronic structure calculations for the solutes of interest.

5.7.2 Solute diffusion

The consideration of solute atoms must include their diffusion. Solutes can jump to any one of its eight nearest sites with jump rate:

$$j_s = z\nu_0 exp(-\frac{F_v}{kT})exp(-\frac{\Delta F_m}{kT}) \tag{5.35}$$

where F_v and ΔF_m are the vacancy formation and solute migration free energies,$z = 1/8$, and ν_0 is the jump frequency. The exponential in eq.5.35 represents the local vacancy concentration, which only depends on the pressure. Since a screw dislocation has no volumetric stress field, we can assume that F_v is independent with stress. The second exponential in the equation represents the vacancy-solute exchange.

ΔF_m is defined as: $\Delta F_m = \Delta E_m - \Delta W_m^s - T\Delta S_m$

Neglecting, as above, the entropic contribution, the mechanical work in this case is: $\Delta W_m^s = \sigma_s : V^*$,where σ_s is the stress tensor at the solute, which contains contributions form the applied stress and the stress field from the dislocation. The latter can be obtained as in eqs.5.28 and 5.29, summing the contrbutions of each segment and using $R_a = \|\mathbf{r}\|$. Alternatively, we can assume an effective *straight* dislocation, where R_a in that case is equal to the distance between the solute and the effective straight line. For its part, V^* is the activation volume tensor whose components are:$V_{ij}^* = \frac{\partial E_m}{\partial \sigma_{ij}}$.

Ideally, E_m and all the V_{ij}^* can be computed using electronic structure calculations. A cheap alternative is to assume that the stress field of a screw dislocation has no volumetric components and therefore has a weak interaction with point sources of dilatation. In this fashion, the effect of the dislocation stress field on the solute migration energy is neglected.

Once eq.5.35 is fully characterized, defect diffusion is carried out on equal footing with any of the other thermally activated processes we already have.

Bibliography

[1] Abdullah Alkhamees, Yue-Lin Liu, Hong-Bo Zhou, Shuo Jin, Ying Zhang, and Guang-Hong Lu. First-principles investigation on dissolution and diffusion of oxygen in tungsten. *J. Nucl. Mater.*, 393(3):508 – 512, 2009.

[2] Garani Ananthakrishna. Current theoretical approaches to collective behavior of dislocations. *Physics reports*, 440(4-6):113–259, 2007.

[3] Ali Argon. *Strengthening mechanisms in crystal plasticity*, volume 4. Oxford University Press on Demand, 2008.

[4] JD Baird. The effects of strain-ageing due to interstitial solutes on the mechanical properties of metals. *Metall. Rev.*, 16(1):1–18, 1971.

[5] Bakaev. Ab initio study of interaction of helium with edge and screw dislocations in tungsten. *Nucl. Instrum. Methods in Phys. Res., Sect. B: Beam Interactions with Materials and Atoms*, 393:150–154, 2017.

[6] Caroline Barouh, Thomas Schuler, Chu-Chun Fu, and Thomas Jourdan. Predicting vacancy-mediated diffusion of interstitial solutes in α-fe. *Phys. Rev. B*, 92:104102, Sep 2015.

[7] CS Becquart and C Domain. An object kinetic monte carlo simulation of the dynamics of helium and point defects in tungsten. *Journal of Nuclear Materials*, 385(2):223–227, 2009.

[8] P. E. Blöchl. Projector augmented-wave method. *Phys. Rev. B: Condens. Matter*, 50:17953–17979, Dec 1994.

[9] H Bolt, V Barabash, G Federici, J Linke, A Loarte, J Roth, and K Sato. Plasma facing and high heat flux materials–needs for iter and beyond. *Journal of Nuclear Materials*, 307:43–52, 2002.

[10] Dieter Brunner. Temperature dependence of the plastic flow of high-purity tungsten single crystals: Dedicated to professor dr. dr. hc alfred seeger on the occasion of his birthday. *International Journal of Materials Research*, 101(8):1003–1013, 2010.

[11] RT Bryant. The solubility of oxygen in transition metal alloys. *Journal of the Less common Metals*, 4(1):62–68, 1962.

[12] JM Brzeski, JE Hack, R Darolia, and RD Field. Strain aging embrittlement of the ordered intermetallic compound nial. *Materials Science and Engineering: A*, 170(1-2):11–18, 1993.

[13] R. Butz and H. Wagner. Diffusion of oxygen on tungsten (110). *Surface Science*, 63:448 – 459, 1977.

[14] Wei Cai, Vasily V Bulatov, and Sidney Yip. Kinetic monte carlo method for dislocation glide in silicon. *Journal of computer-aided materials design*, 6(2):175–183, 1999.

[15] Wei Cai, Vasily V Bulatov, Sidney Yip, and Ali S Argon. Kinetic monte carlo modeling of dislocation motion in bcc metals. *Materials Science and Engineering: A*, 309:270–273, 2001.

[16] D Caillard. Kinetics of dislocations in pure fe. part ii. in situ straining experiments at low temperature. *Acta Materialia*, 58(9):3504–3515, 2010.

[17] D Caillard. An in situ study of hardening and softening of iron by carbon interstitials. *Acta Materialia*, 59(12):4974–4989, 2011.

[18] Daniel Caillard. Dynamic strain ageing in iron alloys: the shielding effect of carbon. *Acta Materialia*, 112:273–284, 2016.

[19] Daniel Caillard and J Bonneville. Dynamic strain aging caused by a new peierls mechanism at high-temperature in iron. *Scripta Materialia*, 95:15–18, 2015.

[20] David Cereceda, Martin Diehl, Franz Roters, Dierk Raabe, J Manuel Perlado, and Jaime Marian. Unraveling the temperature dependence of the yield strength in single-crystal tungsten using atomistically-informed crystal plasticity calculations. *International Journal of Plasticity*, 78:242–265, 2016.

[21] Emmanuel Clouet, Sébastien Garruchet, Hoang Nguyen, Michel Perez, and Charlotte S Becquart. Dislocation interaction with c in α-fe: A comparison between atomic simulations and elasticity theory. *Acta Mater.*, 56(14):3450–3460, 2008.

[22] Emmanuel Clouet, Lisa Ventelon, and François Willaime. Dislocation core energies and core fields from first principles. *Phys. Rev. Lett.*, 102(5):055502, 2009.

[23] Ao H Cottrell and BA Bilby. Dislocation theory of yielding and strain ageing of iron. *Proceedings of the Physical Society. Section A*, 62(1):49, 1949.

[24] Jiten Das, M Sankaranarayana, and TK Nandy. Serrated flow behavior in tungsten heavy alloy. *Mater. Sci. Eng., A*, 646:75–81, 2015.

[25] Joseph R Davis. *Alloying: understanding the basics*. ASM international, 2001.

[26] JW Davis, VR Barabash, A Makhankov, L Plöchl, and KT Slattery. Assessment of tungsten for use in the iter plasma facing components. *Journal of nuclear materials*, 258:308–312, 1998.

[27] C S Deo and D J Srolovitz. First passage time markov chain analysis of rare events for kinetic monte carlo: double kink nucleation during dislocation glide. *Modelling and Simulation in Materials Science and Engineering*, 10(5):581, 2002.

[28] Chaitanya S Deo, David J Srolovitz, Wei Cai, and Vasily V Bulatov. Kinetic monte carlo method for dislocation migration in the presence of solute. *Physical Review B*, 71(1):014106, 2005.

[29] C.S. Deo, D.J. Srolovitz, W. Cai, and V.V. Bulatov. Stochastic simulation of dislocation glide in tantalum and ta-based alloys. *Journal of the Mechanics and Physics of Solids*, 53(6):1223 – 1247, 2005.

[30] CS Deo, DJ Srolovitz, W Cai, and VV Bulatov. Stochastic simulation of dislocation glide in tantalum and ta-based alloys. *Journal of the Mechanics and Physics of Solids*, 53(6):1223–1247, 2005.

[31] L Dezerald, L Proville, Lisa Ventelon, F Willaime, and D Rodney. First-principles prediction of kink-pair activation enthalpy on screw dislocations in bcc transition metals: V, nb, ta, mo, w, and fe. *Physical Review B*, 91(9):094105, 2015.

[32] L. Dezerald, L. Ventelon, E. Clouet, C. Denoual, D. Rodney, and F. Willaime. Ab initio modeling of the two-dimensional energy landscape of screw dislocations in bcc transition metals. *Phys. Rev. B: Condens. Matter*, 89:024104, 2014.

[33] MS Duesbery, V Vitek, and David Keith Bowen. The effect of shear stress on the screw dislocation core structure in body-centred cubic lattices. *Proc. R. Soc. Lond. A*, 332(1588):85–111, 1973.

[34] Juan V Escobar and Isaac Pérez Castillo. Intermittent dynamics in complex systems driven to depletion. *Scientific reports*, 8(1):4825, 2018.

[35] M. Faleschini, H. Kreuzer, D. Kiener, and R. Pippan. Fracture toughness investigations of tungsten alloys and {SPD} tungsten alloys. *Journal of Nuclear Materials*, 367–370, Part A:800 – 805, 2007. Proceedings of the Twelfth International Conference on Fusion Reactor Materials (ICFRM-12)Proceedings of the Twelfth International Conference on Fusion Reactor Materials (ICFRM-12).

[36] M Faleschini, H Kreuzer, D Kiener, and R Pippan. Fracture toughness investigations of tungsten alloys and spd tungsten alloys. *Journal of Nuclear Materials*, 367:800–805, 2007.

[37] SP Fitzgerald and D Nguyen-Manh. Peierls potential for crowdions in the bcc transition metals. *Physical review letters*, 101(11):115504, 2008.

[38] W Frank, HJ Engell, and A Seeger. Migration energy and solubility of oxygen in body centered cubic iron. *Z. Metallkd.*, 58(7):452–455, 1967.

[39] W Frank, HJ Engell, and A Seeger. Solubility and interstitial migration of oxygen in bcc iron. *Trans. Metall. Soc. AIME*, 242(4), 1968.

[40] A Giannattasio, M Tanaka, TD Joseph, and SG Roberts. An empirical correlation between temperature and activation energy for brittle-to-ductile transitions in single-phase materials. *Physica Scripta*, 2007(T128):87, 2007.

[41] A Giannattasio, Z Yao, E Tarleton, and SG Roberts. Brittle–ductile transitions in polycrystalline tungsten. *Philosophical Magazine*, 90(30):3947–3959, 2010.

[42] R. Gibala and T.E. Mitchell. Solid solution softening and hardening. *Scripta Metallurgica*, 7(11):1143 – 1148, 1973.

[43] R Gibala and TE Mitchell. Solid-solution softening and hardening. Technical report, Case Western Reserve Univ., Cleveland, 1973.

[44] B. Gludovatz, S. Wurster, A. Hoffmann, and R. Pippan. Fracture toughness of polycrystalline tungsten alloys. *International Journal of Refractory Metals and Hard Materials*, 28(6):674 – 678, 2010. Selected papers of the 17th International Plansee Seminar 2010 in Reutte, Austria: Tungsten and Molybdenum.

[45] A Greco, P Chuychai, WH Matthaeus, S Servidio, and P Dmitruk. Intermittent mhd structures and classical discontinuities. *Geophysical Research Letters*, 35(19), 2008.

[46] R Gröger, AG Bailey, and V Vitek. Multiscale modeling of plastic deformation of molybdenum and tungsten: I. atomistic studies of the core structure and glide of 1/2¡ 111¿ screw dislocations at 0k. *Acta Materialia*, 56(19):5401–5411, 2008.

[47] Metals Handbook. Vol. 2-properties and selection: Nonferrous alloys and special-purpose mater. *ASM Inter.,*, pages 1119–1124, 1990.

[48] T Hirai, G Pintsuk, J Linke, and M Batilliot. Cracking failure study of iter-reference tungsten grade under single pulse thermal shock loads at elevated temperatures. *Journal of Nuclear Materials*, 390:751–754, 2009.

[49] MZ Hossain and Jaime Marian. Stress-dependent solute energetics in w–re alloys from first-principles calculations. *Acta Materialia*, 80:107–117, 2014.

[50] MZ Hossain and Jaime Marian. Stress-dependent solute energetics in w–re alloys from first-principles calculations. *Acta Mater.*, 80:107–117, 2014.

[51] Yong-Jie Hu, Michael R. Fellinger, Brady G. Bulter, Yi Wang, Kristopher A. Darling, Laszlo J. Kecskes, Dallas R. Trinkle, and Zi-Kui Liu. Solute-induced solid-solution softening and hardening in bcc tungsten. *Acta Materialia*, 141(Supplement C):304 – 316, 2017.

[52] M. Itakura, H. Kaburaki, and M. Yamaguchi. First-principles study on the mobility of screw dislocations in bcc iron. *Acta Mater.*, 60(9):3698–3710, 2012.

[53] M Itakura, H Kaburaki, M Yamaguchi, and T Okita. The effect of hydrogen atoms on the screw dislocation mobility in bcc iron: A first-principles study. *Acta Mater.*, 61(18):6857–6867, 2013.

[54] A. J. JACOBS. Diffusion of oxygen in tungsten and some other transition metals. *Nature*, 200:1310 EP –, 12 1963.

[55] G Janeschitz, Iter Jct, et al. Plasma–wall interaction issues in iter. *Journal of Nuclear Materials*, 290:1–11, 2001.

[56] D. E. Jiang and Emily A. Carter. Diffusion of interstitial hydrogen into and through bcc fe from first principles. *Phys. Rev. B*, 70:064102, Aug 2004.

[57] DE Jiang and Emily A Carter. Diffusion of interstitial hydrogen into and through bcc fe from first principles. *Physical Review B*, 70(6):064102, 2004.

[58] Reiner Kirchheim. Solid solution softening and hardening by mobile solute atoms with special focus on hydrogen. *Scripta Materialia*, 67(9):767 – 770, 2012.

[59] Motomichi Koyama, Takahiro Sawaguchi, and Kaneaki Tsuzaki. Influence of dislocation separation on dynamic strain aging in a fe–mn–c austenitic steel. *Materials Transactions*, 53(3):546–552, 2012.

[60] G. Kresse and J. Hafner. *Phys. Rev. B: Condens. Matter*, 47:558, 1993.

[61] G. Kresse and D. Joubert. From ultrasoft pseudopotentials to the projector augmented-wave method. *Phys. Rev. B: Condens. Matter*, 59:1758–1775, Jan 1999.

[62] Subodh Kumar, Erwin Pink, and Robert Grill. Dynamic strain aging in a tungsten heavy metal. *Scripta materialia*, 35(9):1047–1052, 1996.

[63] Erik Lassner and Wolf-Dieter Schubert. Properties, chemistry, technology of the element, alloys, and chemical compounds. *Vienna University of Technology, Vienna, Austria, Kluwer*, pages 124–125, 1999.

[64] Erik Lassner and Wolf-Dieter Schubert. Tungsten alloys. In *Tungsten*, pages 255–282. Springer, 1999.

[65] C. H. LEE. Oxygen diffusion in tungsten. *Nature*, 203:1163, 09 1964.

[66] W. C. Leslie. Iron and its dilute substitutional solid solutions. *Metallurgical Transactions*, 3(1):5–26, Jan 1972.

[67] Gerard Paul M Leyson, William A Curtin, Louis G Hector Jr, and Christopher F Woodward. Quantitative prediction of solute strengthening in aluminium alloys. *Nature materials*, 9(9):750, 2010.

[68] Hong Li, Claudia Draxl, Stefan Wurster, Reinhard Pippan, and Lorenz Romaner. Impact of *d*-band filling on the dislocation properties of bcc transition metals: The case of tantalum-tungsten alloys investigated by density-functional theory. *Phys. Rev. B*, 95:094114, Mar 2017.

[69] Hong Li, Stefan Wurster, Christian Motz, Lorenz Romaner, Claudia Ambrosch-Draxl, and Reinhard Pippan. Dislocation-core symmetry and slip planes in tungsten alloys: Ab initio calculations and microcantilever bending experiments. *Acta Mater.*, 60(2):748–758, 2012.

[70] Jifeng Li, Ignacio Romero, and Javier Segurado. Development of a thermo-mechanically coupled crystal plasticity modeling framework: application to polycrystalline homogenization. *arXiv preprint arXiv:1903.03593*, 2019.

[71] Ruihuan Li, Pengbo Zhang, Xiaoqing Li, Chong Zhang, and Jijun Zhao. First-principles study of the behavior of o, n and c impurities in vanadium solids. *J. Nucl. Mater.*, 435(1-3):71–76, 2013.

[72] TQ Li, YB Liu, ZY Cao, RZ Wu, ML Zhang, LR Cheng, and DM Jiang. The twin mechanism of portevin le chatelier in mg–5li–3al–1.5 zn–2re alloy. *Journal of Alloys and Compounds*, 509(28):7607–7610, 2011.

[73] Lu. A review of modelling and simulation of hydrogen behaviour in tungsten at different scales. *Nucl. Fusion*, 54(8):086001, 2014.

[74] A Luo, DL Jacobson, and KS Shin. Solution softening mechanism of iridium and rhenium in tungsten at room temperature. *International Journal of Refractory Metals and Hard Materials*, 10(2):107–114, 1991.

[75] A. Luo, D.L. Jacobson, and K.S. Shin. Solution softening mechanism of iridium and rhenium in tungsten at room temperature. *International Journal of Refractory Metals and Hard Materials*, 10(2):107 – 114, 1991.

[76] B Lüthi, L Ventelon, C Elsässer, D Rodney, and F Willaime. First principles investigation of carbon-screw dislocation interactions in body-centered cubic metals. *Modelling and Simulation in Materials Science and Engineering*, 25(8):084001, 2017.

[77] B. Lüthi, L. Ventelon, D. Rodney, and F. Willaime. Attractive interaction between interstitial solutes and screw dislocations in bcc iron from first principles. *Comput. Mater. Sci.*, 148:21 – 26, 2018.

[78] B. Lüthi, L. Ventelon, D. Rodney, and F. Willaime. Attractive interaction between interstitial solutes and screw dislocations in bcc iron from first principles. *Comput. Mater. Sci.*, 148:21 – 26, 2018.

[79] B Lüthi, L Ventelon, D Rodney, and F Willaime. Attractive interaction between interstitial solutes and screw dislocations in bcc iron from first principles. *Computational Materials Science*, 148:21–26, 2018.

[80] S Mahajan, D Brasen, and P Haasen. Lüders bands in deformed silicon crystals. *Acta Metallurgica*, 27(7):1165–1173, 1979.

[81] J Marian and A Caro. Moving dislocations in disordered alloys: Connecting continuum and discrete models with atomistic simulations. *Physical Review B*, 74(2):024113, 2006.

[82] Jaime Marian, Wei Cai, and Vasily V Bulatov. Dynamic transitions from smooth to rough to twinning in dislocation motion. *Nature materials*, 3(3):158, 2004.

[83] Cecile Marichal, Helena Van Swygenhoven, Steven Van Petegem, and Camelia Borca. {110} slip with {112} slip traces in bcc tungsten. *Scientific reports*, 3:2547, 2013.

[84] Enrique Martínez, María José Caturla, and Jaime Marian. Dft-parameterized object kinetic monte carlo simulations of radiation damage. *Handbook of Materials Modeling: Applications: Current and Emerging Materials*, pages 1–32, 2018.

[85] Enrique Martínez, Daniel Schwen, and Alfredo Caro. Helium segregation to screw and edge dislocations in α-iron and their yield strength. *Acta Materialia*, 84:208–214, 2015.

[86] PG McCormick, S Venkadesan, and CP Ling. Propagative instabilities: an experimental view. *Scripta Metallurgica et Materialia;(United States)*, 29(9), 1993.

[87] NI Medvedeva, Yu N Gornostyrev, and AJ Freeman. Solid solution softening and hardening in the group-v and group-vi bcc transition metals alloys: First principles calculations and atomistic modeling. *Phys. Rev. B: Condens. Matter*, 76(21):212104, 2007.

[88] Y. Mutoh, K. Ichikawa, K. Nagata, and M. Takeuchi. Effect of rhenium addition on fracture toughness of tungsten at elevated temperatures. *Journal of Materials Science*, 30(3):770–775, 1995.

[89] Sia Nemat-Nasser and Wei-Guo Guo. Thermomechanical response of hsla-65 steel plates: experiments and modeling. *Mechanics of Materials*, 37(2-3):379–405, 2005.

[90] H Neuhäuser and A Hampel. Observation of lüders bands in single crystals. *Scripta Metallurgica et Materialia;(United States)*, 29(9), 1993.

[91] Duc Nguyen-Manh. Ab-initio modelling of point defect-impurity interaction in tungsten and other bcc transition metals. In *1st International Conference On New Materials for Extreme Environment*, volume 59 of *Advanced Materials Research*, pages 253–256. Trans Tech Publications, 2 2009.

[92] M Niinomi, T Kobayashi, and K Ikeda. Portevinle chatelier effect in al-si binary alloys. *Journal of materials science letters*, 5(9):847–848, 1986.

[93] H Numakura and M Koiwa. The snoek relaxation in dilute ternary bcc alloys. a review. *Le Journal de Physique IV*, 6(C8):C8–97, 1996.

[94] K. Okazaki. Solid-solution hardening and softening in binary iron alloys. *Journal of Materials Science*, 31(4):1087–1099, Jan 1996.

[95] David L Olmsted, Louis G Hector Jr, and WA Curtin. Molecular dynamics study of solute strengthening in al/mg alloys. *Journal of the Mechanics and Physics of Solids*, 54(8):1763–1788, 2006.

[96] J Pamela, A Bécoulet, D Borba, J-L Boutard, L Horton, and D Maisonnier. Efficiency and availability driven r&d issues for demo. *Fusion Engineering and Design*, 84(2-6):194–204, 2009.

[97] Stefanos Papanikolaou, Felipe Bohn, Rubem Luis Sommer, Gianfranco Durin, Stefano Zapperi, and James P Sethna. Universality beyond power laws and the average avalanche shape. *Nature Physics*, 7(4):316, 2011.

[98] SC Park, LP Beckerman, and RE Reed-Hill. On the portevin-le chatelier effect due to snoek strain aging in the niobium oxygen system. *Metallurgical Transactions A*, 14(2):463–469, 1983.

[99] RC Picu. A mechanism for the negative strain-rate sensitivity of dilute solid solutions. *Acta Materialia*, 52(12):3447–3458, 2004.

[100] Erwin Pink and Richard J. Arsenault. Low-temperature softening in body-centered cubic alloys. *Progress in Materials Science*, 24(Supplement C):1 – 50, 1980.

[101] Erwin Pink and Richard J Arsenault. Low-temperature softening in body-centered cubic alloys. *Progress in Materials Science*, 24:1–50, 1980.

[102] Giacomo Po, Yinan Cui, David Rivera, David Cereceda, Tom D Swinburne, Jaime Marian, and Nasr Ghoniem. A phenomenological dislocation mobility law for bcc metals. *Acta Materialia*, 119:123–135, 2016.

[103] M Pozuelo, YW Chang, J Marian, and JM Yang. Serrated flow in nanostructured binary mg-al alloys. *Scripta Materialia*, 127:178–181, 2017.

[104] Marta Pozuelo, Jacob W Stremfel, Jenn-Ming Yang, and Jaime Marian. Strengthening to softening transition in lath martensite. *Materialia*, 5:100254, 2019.

[105] Peter L Raffo. Yielding and fracture in tungsten and tungsten-rhenium alloys. *Journal of the Less Common Metals*, 17(2):133–149, 1969.

[106] EJ Rapperport, Victor Nerses, and MF Smith. Diffusion in refractory metals. Technical report, TEXTRON INC WEST CONCORD MA NUCLEAR METALS DIV, 1964.

[107] K.V. Ravi and R. Gibala. The strength and alloy softening of bcc metals. *Scripta Metallurgica*, 3(8):547 – 551, 1969.

[108] K.V Ravi and R Gibala. The strength of niobium-oxygen solid solutions. *Acta Metallurgica*, 18(6):623 – 634, 1970.

[109] JM Rickman, R LeSar, and DJ Srolovitz. Solute effects on dislocation glide in metals. *Acta materialia*, 51(5):1199–1210, 2003.

[110] M Rieth, SL Dudarev, SM Gonzalez De Vicente, J Aktaa, T Ahlgren, S Antusch, DEJ Armstrong, M Balden, N Baluc, M-F Barthe, et al. Recent progress in research on tungsten materials for nuclear fusion applications in europe. *Journal of Nuclear Materials*, 432(1-3):482–500, 2013.

[111] E Rodary, D Rodney, L Proville, Y Bréchet, and G Martin. Dislocation glide in model ni (al) solid solutions by molecular dynamics. *Physical Review B*, 70(5):054111, 2004.

[112] D Rodney, L Ventelon, E Clouet, L Pizzagalli, and F Willaime. Ab initio modeling of dislocation core properties in metals and semiconductors. *Acta Mater.*, 124:633–659, 2017.

[113] L Romaner, VI Razumovskiy, and R Pippan. Core polarity of screw dislocations in fe–co alloys. *Phil. Mag. Lett.*, 94(6):334–341, 2014.

[114] Lorenz Romaner, Claudia Ambrosch-Draxl, and Reinhard Pippan. Effect of rhenium on the dislocation core structure in tungsten. *Physical review letters*, 104(19):195503, 2010.

[115] Franz Roters, Philip Eisenlohr, Luc Hantcherli, Denny Dharmawan Tjahjanto, Thomas R Bieler, and Dierk Raabe. Overview of constitutive laws, kinematics, homogenization and multiscale methods in crystal plasticity finite-element modeling: Theory, experiments, applications. *Acta Materialia*, 58(4):1152–1211, 2010.

[116] Joachim Roth, E Tsitrone, A Loarte, Th Loarer, G Counsell, R Neu, V Philipps, S Brezinsek, M Lehnen, P Coad, et al. Recent analysis of key plasma wall interactions issues for iter. *Journal of Nuclear Materials*, 390:1–9, 2009.

[117] Gerardo Rubino, Bruno Tuffin, et al. *Rare event simulation using Monte Carlo methods*, volume 73. Wiley Online Library, 2009.

[118] G D Samolyuk, Y N Osetsky, and R E Stoller. The influence of transition metal solutes on the dislocation core structure and values of the peierls stress and barrier in tungsten. *Journal of Physics: Condensed Matter*, 25(2):025403, 2013.

[119] German D Samolyuk, YN Osetsky, and RE Stoller. The influence of transition metal solutes on the dislocation core structure and values of the peierls stress and barrier in tungsten. *Journal of Physics: Condensed Matter*, 25(2):025403, 2012.

[120] J Sanchez, J Fullea, MC Andrade, and PL De Andres. Ab initio molecular dynamics simulation of hydrogen diffusion in α-iron. *Physical Review B*, 81(13):132102, 2010.

[121] A Sato and M Meshii. Solid solution softening and solid solution hardening. *Acta Metallurgica*, 21(6):753 – 768, 1973.

[122] G Schoeck and A Seeger. The flow stress of iron and its dependence on impurities. *Acta metallurgica*, 7(7):469–477, 1959.

[123] A Seeger. The temperature and strain-rate dependence of the flow stress of body-centred cubic metals: A theory based on kink–kink interactions. *Zeitschrift fur Metallkunde*, 72(6):369–380, 1981.

[124] SL Shang, HZ Fang, J Wang, CP Guo, Y Wang, PD Jablonski, Y Du, and ZK Liu. Vacancy mechanism of oxygen diffusivity in bcc fe: A first-principles study. *Corros. Sci.*, 83:94–102, 2014.

[125] V.K. Sikka and C.J. Rosa. The oxidation kinetics of tungsten and the determination of oxygen diffusion coefficient in tungsten trioxide. *Corrosion Science*, 20(11):1201 – 1219, 1980.

[126] RL Smialek and TE Mitchell. Interstitial solution hardening in tantalum single crystals. *Philos. Mag.*, 22(180):1105–1127, 1970.

[127] DF Stein and JR Low Jr. Effects of orientation and carbon on the mechanical properties of iron single crystals. *Acta Metall.*, 14(10):1183–1194, 1966.

[128] Joseph R Stephens. Effect of oxygen on mechanical properties of tungsten. Technical report, NATIONAL AERONAUTICS AND SPACE ADMINISTRATION CLEVELAND OH LEWIS RESEARCH CENTER, 1963.

[129] Joseph R Stephens. Effects of interstitial impurities on the low-temperature tensile properties of tungsten. Technical report, NATIONAL AERONAUTICS AND SPACE ADMINISTRATION CLEVELAND OH LEWIS RESEARCH CENTER, 1964.

[130] Joseph R. Stephens. Dislocation structures in single-crystal tungsten and tungsten alloys. *Metallurgical and Materials Transactions*, 1(5):1293–1301, 1970.

[131] Joseph R Stephens. Dislocation structures in single-crystal tungsten and tungsten alloys. *Metallurgical and Materials Transactions B*, 1(5):1293–1301, 1970.

[132] Alexander Stukowski. Visualization and analysis of atomistic simulation data with ovito–the open visualization tool. *Modelling and Simulation in Materials Science and Engineering*, 18(1):015012, 2009.

[133] Alexander Stukowski, David Cereceda, Thomas D Swinburne, and Jaime Marian. Thermally-activated non-schmid glide of screw dislocations in w using atomistically-informed kinetic monte carlo simulations. *International Journal of Plasticity*, 65:108–130, 2015.

[134] A Karimi Taheri, Maccagno TM, and Jonas JJ. Dynamic strain aging and the wire drawing of low carbon steel rods. *ISIJ international*, 35(12):1532–1540, 1995.

[135] Meijie Tang and Jaime Marian. Temperature and high strain rate dependence of tensile deformation behavior in single-crystal iron from dislocation dynamics simulations. *Acta Materialia*, 70:123–129, 2014.

[136] Thomas Edwin Tietz and Jess W Wilson. Behavior and properties of refractory metals. 1965.

[137] Dallas R. Trinkle. Diffusivity and derivatives for interstitial solutes: activation energy, volume, and elastodiffusion tensors. *Philosophical Magazine*, 96(26):2714–2735, 2016.

[138] Dallas R. Trinkle and Christopher Woodward. The chemistry of deformation: How solutes soften pure metals. *Science*, 310(5754):1665–1667, 2005.

[139] Dallas R Trinkle and Christopher Woodward. The chemistry of deformation: How solutes soften pure metals. *Science*, 310(5754):1665–1667, 2005.

[140] MG Ulitchny and R Gibala. The effects of interstitial solute additions on the mechanical properties of niobium and tantalum single crystals. *Journal of the Less Common Metals*, 33(1):105–116, 1973.

[141] RGA Veiga, H Goldenstein, M Perez, and CS Becquart. Monte carlo and molecular dynamics simulations of screw dislocation locking by cottrell atmospheres in low carbon fe–c alloys. *Scr. Mater.*, 108:19–22, 2015.

[142] RGA Veiga, Michel Perez, CS Becquart, E Clouet, and C Domain. Comparison of atomistic and elasticity approaches for carbon diffusion near line defects in α-iron. *Acta Materialia*, 59(18):6963–6974, 2011.

[143] L. Ventelon and F. Willaime. Generalized stacking-faults and screw-dislocation core-structure in bcc iron: a comparison between ab initio calculations and empirical potentials. *Philos. Mag.*, 90:1063–1074, 2010.

[144] L. Ventelon, F. Willaime, E. Clouet, and D. Rodney. Ab initio investigation of the peierls potential of screw dislocations in bcc fe and w. *Acta Mater.*, 61(11):3973 – 3985, 2013.

[145] Lisa Ventelon, B Lüthi, E Clouet, L Proville, B Legrand, D Rodney, and F Willaime. Dislocation core reconstruction induced by carbon segregation in bcc iron. *Phys. Rev. B: Condens. Matter*, 91(22):220102, 2015.

[146] Lisa Ventelon, B. Lüthi, E. Clouet, L. Proville, B. Legrand, D. Rodney, and F. Willaime. Dislocation core reconstruction induced by carbon segregation in bcc iron. *Phys. Rev. B: Condens. Matter*, 91:220102, Jun 2015.

[147] V Vitek. Structure of dislocation cores in metallic materials and its impact on their plastic behaviour. *Progress in materials science*, 36:1–27, 1992.

[148] V Vitek, RC Perrin, and DK Bowen. The core structure of 1/2 (111) screw dislocations in bcc crystals. *Philos. Mag.*, 21(173):1049–1073, 1970.

[149] Guofeng Wang, Nitia Ramesh, Andrew Hsu, Deryn Chu, and Rongrong Chen. Density functional theory study of the adsorption of oxygen molecule on iron phthalocyanine and cobalt phthalocyanine. *Molecular Simulation*, 34(10-15):1051–1056, 2008.

[150] Y Wang, DJ Srolovitz, JM Rickman, and R Lesar. Dislocation motion in the presence of diffusing solutes: A computer simulation study. *Acta materialia*, 48(9):2163–2175, 2000.

[151] C. R. Weinberger, G. J. Tucker, and S. M. Foiles. Peierls potential of screw dislocations in bcc transition metals: Predictions from density functional theory. *Phys. Rev. B: Condens. Matter*, 87(5):054114, 2013.

[152] Alexander Frank Wells. *Structural inorganic chemistry*. Oxford university press, 2012.

[153] BA Wilcox and GC Smith. The portevin-le chatelier effect in hydrogen charged nickel. *Acta Metallurgica*, 12(4):371–376, 1964.

[154] Stefan Wurster, Bernd Gludovatz, and Reinhard Pippan. High temperature fracture experiments on tungsten–rhenium alloys. *International Journal of Refractory Metals and Hard Materials*, 28(6):692–697, 2010.

[155] Wei Xu and John Moriarty. Atomistic simulation of ideal shear strength, point defects, and screw dislocations in bcc transition metals: Mo as a prototype. *Physical Review B*, 54:6941, 09 1996.

[156] Joseph A. Yasi, Louis G. Hector, and Dallas R. Trinkle. First-principles data for solid-solution strengthening of magnesium: From geometry and chemistry to properties. *Acta Materialia*, 58(17):5704 – 5713, 2010.

[157] H Yoshinaga, K Toma, K Abe, and S Morozumi. The portevin-le chatelier effect in vanadium. *The Philosophical Magazine: A Journal of Theoretical Experimental and Applied Physics*, 23(186):1387–1403, 1971.

[158] B Zhao, C Shang, N Qi, ZY Chen, and ZQ Chen. Stability of defects in monolayer mos2 and their interaction with o2 molecule: A first-principles study. *Applied Surface Science*, 412:385–393, 2017.

[159] Yi Zhao and Gang Lu. Qm/mm study of dislocation—hydrogen/helium interactions in α-fe. *Modell. Simul. in Mater. Sci. Eng.*, 19(6):065004, 2011.

[160] Yue Zhao, Lucile Dezerald, and Jaime Marian. Electronic structure calculations of oxygen atom transport energetics in the presence of screw dislocations in tungsten. *Metals*, 9(2):252, 2019.

[161] Yue Zhao and Jaime Marian. Direct prediction of the solute softening-to-hardening transition in w–re alloys using stochastic simulations of screw dislocation motion. *Modell. Simul. in Mater. Sci. Eng.*, 26(4):045002, 2018.

[162] Yue Zhao and Jaime Marian. Direct prediction of the solute softening-to-hardening transition in w–re alloys using stochastic simulations of screw dislocation motion. *Modelling and Simulation in Materials Science and Engineering*, 26(4):045002, 2018.

[163] SJ Zinkle and NM Ghoniem. Operating temperature windows for fusion reactor structural materials. *Fusion Engineering and design*, 51:55–71, 2000.